

Neutral atomic and molecular clouds and star formation in the outer Carina arm

GEUMSOOK PARK (박금숙)^{1,2} BON-CHUL KOO,^{3,4} KEE-TAE KIM,¹ AND BRUCE ELMEGREEN⁵

¹*Korea Astronomy and Space Science Institute, 776 Daedeokdae-ro, Yuseong-gu, Daejeon 34055, Republic of Korea*

²*Research Institute of Natural Sciences, Chungnam National University 99 Daehak-ro, Yuseong-gu, Daejeon 34134, Republic of Korea*

³*Department of Physics and Astronomy, Seoul National University, Seoul 08861, Republic of Korea*

⁴*Research Institute of Basic Sciences, Seoul National University, Seoul 08826, Republic of Korea*

⁵*IBM Thomas J. Watson Research Center, Yorktown Heights, New York 10598, USA*

ABSTRACT

We present a comprehensive investigation of H I (super)clouds, molecular clouds (MCs), and star formation in the Carina spiral arm of the outer Galaxy. Utilizing HI4PI and CfA CO survey data, we identify H I clouds and MCs based on the (l, v_{LSR}) locations of the Carina arm. We analyzed 26 H I clouds and 48 MCs. Most of the identified H I clouds are superclouds, with masses exceeding $10^6 M_{\odot}$. We find that 15 of these superclouds have associated MC(s) with $M_{\text{HI}} \gtrsim 10^6 M_{\odot}$ and $\Sigma_{\text{HI+H}_2} \gtrsim 50 M_{\odot} \text{pc}^{-2}$. Our virial equilibrium analysis suggests that these CO-bright H I clouds are gravitationally bound or marginally bound. We report an anti-correlation between molecular mass fractions and Galactocentric distances, and a correlation with total gas surface densities. Nine CO-bright H I superclouds are associated with H II regions, indicating ongoing star formation. We confirm the regular spacing of H I superclouds along the spiral arm, which is likely due to some underlying physical process, such as gravitational instabilities. We observe a strong spatial correlation between H II regions and MCs, with some offsets between MCs and local H I column density peaks. Our study reveals that in the context of H I superclouds, the star formation rate surface density is independent of H I and total gas surface densities but positively correlates with molecular gas surface density. This finding is consistent with both extragalactic studies of the resolved Kennicutt-Schmidt relation and local giant molecular clouds study of Lada et al. (2013), emphasizing the crucial role of molecular gas in regulating star formation processes.

1. INTRODUCTION

Stars form within the densest regions of molecular clouds, which are predominately found within giant H I clouds, known as H I superclouds (Grabelsky et al. 1987; Elmegreen & Elmegreen 1987; Lada et al. 1988). Star complexes, the largest scale of star-forming regions in galaxies, form within giant molecular clouds (GMCs) inside H I superclouds (Elmegreen 2004). Therefore, the formation of H I superclouds marks the onset of star formation. Understanding the properties of H I superclouds is essential for comprehending global star formation properties in galaxies.

Fukui & Kawamura (2010) reviewed the importance of studying the association between GMCs and H I gas in understanding the formation and evolution of GMCs. They summarized the finding that while GMCs often form in H I filaments, intense H I is not always associated with CO gas. However, the GMC-H I association has not been well established in the Milky Way, leaving room for further investigation. This connection suggests a strong interplay between the atomic and molecular

phases of the interstellar medium, which is crucial for understanding star formation processes.

H I superclouds typically exhibit masses ranging from 10^6 to $10^7 M_{\odot}$ and sizes up to approximately 1 kpc, as reported by various studies such as those by Elmegreen & Elmegreen (1987) and Engargiola et al. (2003). The regular distribution of these superclouds along the spiral arms of galaxies, including the Milky Way, has been well-established through H I observations (e.g., McGee & Milton 1964; Elmegreen & Elmegreen 1983; Boulanger & Viallefond 1992). McGee & Milton (1964) conducted an early study that demonstrated a series of H I superclouds can be observed in the Carina spiral arm in the fourth quadrant of the Milky Way.

According to Grabelsky et al. (1987), there is good agreement between distributions of H I superclouds and molecular clouds (MCs) in spiral arms. However, previous H I surveys with low angular resolution limited the ability to reveal detailed structures of H I superclouds in both space and velocity. The recent all-sky H I 4π (HI4PI) survey (HI4PI Collaboration et al. 2016) pro-

vides a significantly improved angular resolution, offering 3 to 8 times better resolution compared to previous surveys. In this paper, we aim to identify and analyze HI superclouds and GMCs in the longitude range from 288° to 340° at positive velocities, corresponding to the *outer* Carina arm.

The outer Carina arm is a favorite subject for research because it does not have kinematic distance ambiguity, which reduces the likelihood of being influenced by outer spiral arms. Despite this advantage, the outer Carina arm has received limited attention since the 1980s. In this study, we use the locations (l, v_{LSR}) of the outer Carina arm as determined by Koo et al. (2017, hereafter referred to as Paper I) to extract HI emission associated with the spiral arm. Paper I traced the spiral arms in the outer Galaxy using the LAB HI data with a beam size of $30' - 36'$ full-width at half-maximum (FWHM) (Kalberla et al. 2005). The study identified four spiral arms, including the Sagittarius-Carina, Perseus, Outer, and Scutum-Centaurus arms, using a combination of local peak intensities and radial velocities integrated along latitudes. Through the use of (l, v_{LSR}) diagrams of local peak intensities integrated along latitudes, Paper I clearly defined the four spiral arms and prominent interarm features.

Many previous studies have explored the relationships between gas and star formation on both local and extragalactic scales. For example, Bigiel et al. (2008) demonstrated that the star formation rate surface density correlates well with molecular gas surface density but shows little or no correlation with atomic gas surface density in nearby spiral galaxies. Furthermore, Lada et al. (2013) found that star formation rates in local GMCs are independent of total gas surface density, emphasizing the importance of molecular gas in star formation. These results highlight the importance of understanding the properties and distribution of HI superclouds in relation to molecular gas and star-forming regions.

In this paper, we present a comprehensive study of the outer Carina arm, focusing on HI clouds and their relationships with MCs and star-forming regions. Section 2 provides brief descriptions of HI and ^{12}CO (hereafter CO) survey data used in this study. In Section 3, we outline the process of identifying HI clouds and MCs in the outer Carina arm and determining their physical parameters, such as velocity, distance, and mass. We also examine the spatial distribution and virial equilibrium of the HI superclouds identified in this study. Section 4 compares the properties of HI clouds and molecular clouds in the outer Carina arm. In Section 5, we compare the properties of star-forming regions with the two cloud components and analyze the star formation

rates in the HI superclouds. Finally, in Section 6, we summarize our results and draw our conclusions.

2. DATA

2.1. HI Data from the HI4PI Survey

In order to obtain images with a higher angular resolution, we utilize the HI4PI survey (HI4PI Collaboration et al. 2016). This survey combines the Effelsberg-Bonn HI Survey (EBHIS) observed with the 100 m Effelsberg radio telescope in the northern hemisphere (Kerp et al. 2011; Winkel et al. 2016), and the Galactic All-Sky Survey (GASS) collected with the 64 m Parkes telescope in the southern hemisphere (McClure-Griffiths et al. 2009; Kalberla et al. 2010; Kalberla & Haud 2015). The HI4PI survey has an angular resolution of $16'.2$ FWHM and a velocity channel width of 1.29 km s^{-1} , with a brightness temperature noise level of $\sim 43 \text{ mK}$.

During the analysis, we encountered a false absorption-like feature around $(l, b) \sim (291.5^\circ, -0.5^\circ)$ when comparing with other data, such as SGPS data (Parkes multibeam data) (McClure-Griffiths et al. 2005). To address this issue, the erroneous pixels were replaced with the SGPS data. The SGPS data were rebinned and interpolated to match the grid coordinates of the HI4PI data. Additionally, the reprocessed SGPS data were multiplied by 0.956 to account for the slightly different brightness temperature levels, which were obtained by averaging brightness temperature ratios from four neighboring peaks.

2.2. CO Data from the CfA Survey

We use the composite Galactic CO survey data of Dame et al. (2001). The survey is comprised of several large-scale, unbiased surveys using the CfA 1.2 m telescope in the northern hemisphere (with an angular resolution of $8'.4$) and CfA-Chile 1.2 m telescope in the southern hemisphere (with an angular resolution of $8'.8$). The composite CO survey data are grid sampled with a sampling interval of $7'.5$ and a velocity width of 1.3 km s^{-1} . The data for the Galactic 4th quadrant, that are used in this study, provide a main beam temperature noise level of $\sim 0.17 \text{ K}$. To obtain a CO cube with the same angular resolution as the HI data, we employed Gaussian smoothing with a kernel size of $13'.8$ FWHM. Throughout this paper, we utilized the smoothed CO data with an angular resolution of $16'.2$ FWHM for all images and analysis.

3. ATOMIC AND MOLECULAR CLOUDS IN THE OUTER CARINA ARM

3.1. Cloud Identification

In Paper I, we presented systemic LSR velocity information along the outer Carina arm. Figure 1 depicts

three b -integrated (l , v_{LSR}) diagrams of H I local peak intensities as well as ordinary H I and CO emissions. The zigzagging solid lines in the figure denote the locations of the outer Carina arm, which were traced in Paper I. A majority of the emission features associated with the outer Carina arm appear to be distributed between two thick dotted lines, approximately 25 km s^{-1} in width. The spiral arm exhibits clear visible clumpy structures in both H I and CO emissions.

Due to the ubiquitous nature of H I emission, particularly in the Galactic plane, identifying three-dimensional clumps from cube data is challenging. Therefore, our clump identification procedure involved two main steps. In the first step, we determine the projected (l , b) area from a v -integrated image (as discussed in Section 3.1.1). In the second step, we use Gaussian decomposition to measure the mean velocity component(s) of each cloud from the area-averaged spectra (as explained in Section 3.1.2). Although the CO PPV cube is less complex than the H I cube, we employ this method to define MCs for consistency.¹

3.1.1. Step I: Spatial Identification

To identify clumpy structures of the arm, we begin by creating a v -integrated (l , b) diagram using data within a width of approximately 25 km s^{-1} centered at the outer Carina arm traces depicted in Figure 1. The resulting (l , b) diagrams in H I and CO, presented in Figure 2(a), exhibit clumpy structures along Galactic longitudes similar to those shown in earlier studies, such as Figure 6a of McGee & Milton (1964) or Figure 15 of Grabelsky et al. (1987), albeit at a higher resolution. To identify H I clouds and MCs from Figure 2(a), we employ the IDL/CLUMPFIND algorithm (Williams et al. 1994). This algorithm works by contouring an input image from the highest level to the lowest one. The outcome, such as the number and size of clouds, depends sensitively on the input contour levels. To obtain appropriate levels of the v -integrated intensity, we conduct empirical attempts and determine the following: (1210, 1260, 1320, 1430, 1700, 1810, 1850) K km s^{-1} for H I and (2.5, 4.5, 7, 10, 15, 20) K km s^{-1} for CO. The minimum of the H I contour levels corresponds to $N_{\text{HI}} \simeq 2.2 \times 10^{21} \text{ cm}^{-2}$, assuming the line to be optically thin, while the minimum CO threshold is comparable to $N_{\text{H}_2} \simeq 5 \times 10^{20} \text{ cm}^{-2}$. We identify twenty-nine H I clouds and forty-nine MCs along the outer Carina arm, spanning from $l = 288^\circ$

to 340° (see Figure 2(b)). While defining MCs, we try to delineate clumpy structures as individual objects as much as possible, which differs slightly from the identification of H I clouds.

Some H I clouds were found to have abnormal, discontinuous pixels included in the clumpfind-result area. These pixels were manually removed. Additionally, two H I clouds, H2, and H5, were obtained by combining two or three clumpfind-pieces, as they appeared to be connected with each other. On the other hand, we observed that for three H I clouds, H4, H9, and H22, their latitudinal intensity distributions suggest that the identified area is not a significant contributor within the given longitude range. These clouds may be part of a larger cloudy structure. Therefore, we have excluded them from further analysis and discussion, despite the inferred parameters presented in Table 1. As a result, this paper focuses on twenty-six H I clouds.

The process of identifying H I clouds involves defining bright areas against widely-extended diffuse H I emission. On the other hand, the identification of MCs takes into account most of the detectable CO emissions from the given survey data. Almost all of the identified MCs listed in this paper are likely to be associated with the H I clouds mentioned herein. A few MCs located at $l \sim 288^\circ$ to 289° are not included in this paper, as they are associated with other H I emission features that are not explored here. Additionally, we limit the minimum pixel number of MCs to 5, which corresponds to a circle area with a radius of approximately $9/5$.

We examined the presence and overlap of MCs within the identified H I cloud areas and determined the possible association between MCs and H I clouds. Our analysis revealed that 16 cataloged H I clouds are associated with MCs. Among the CO-bright H I clouds, six are matched with single MCs, while ten are matched with two or more MCs. We also found that H9 is associated with the relevant MC (M34), although it was excluded from the statistical analysis. Furthermore, M34 was also excluded from further analysis, resulting in a total of 48 MCs that will be discussed in this paper.

3.1.2. Step II: Gaussian Decomposition

In order to understand the kinematic characteristics of clouds, we attempt to isolate the cloud velocity component(s) using multiple Gaussian fitting from a velocity profile averaged within the identified cloud area in (l , b) space. However, this task is challenging, particularly for H I profiles, due to contamination by different arm or *interarm* components. This complexity results in a mixing of many velocities, making it difficult to determine the number of features present. To

¹ In this study, the identification of clouds is based on the v -integrated map and does not take into account the three-dimensional CO distribution. As a result, multiple components along a line of sight may be merged into a single identified MC.

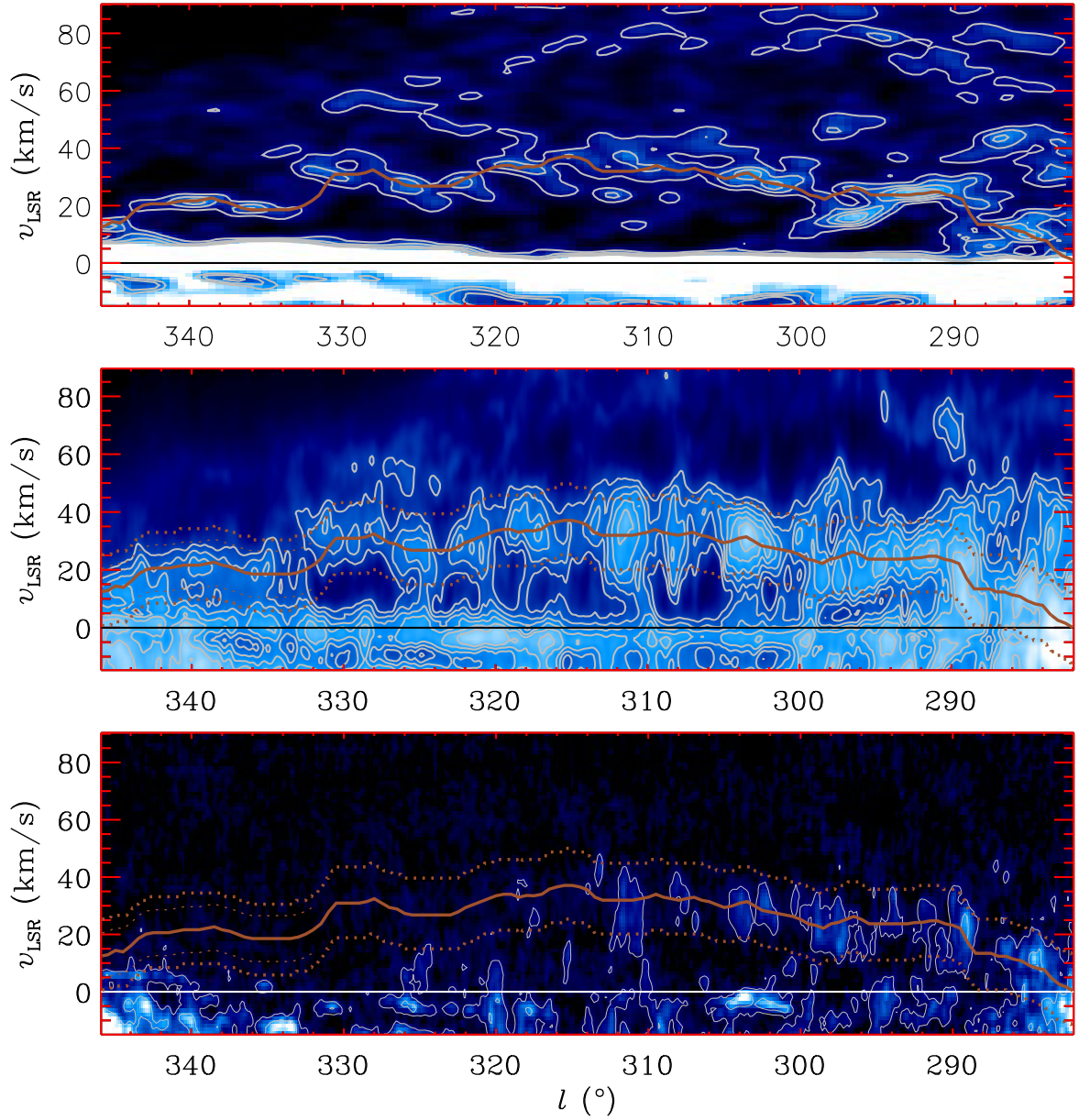
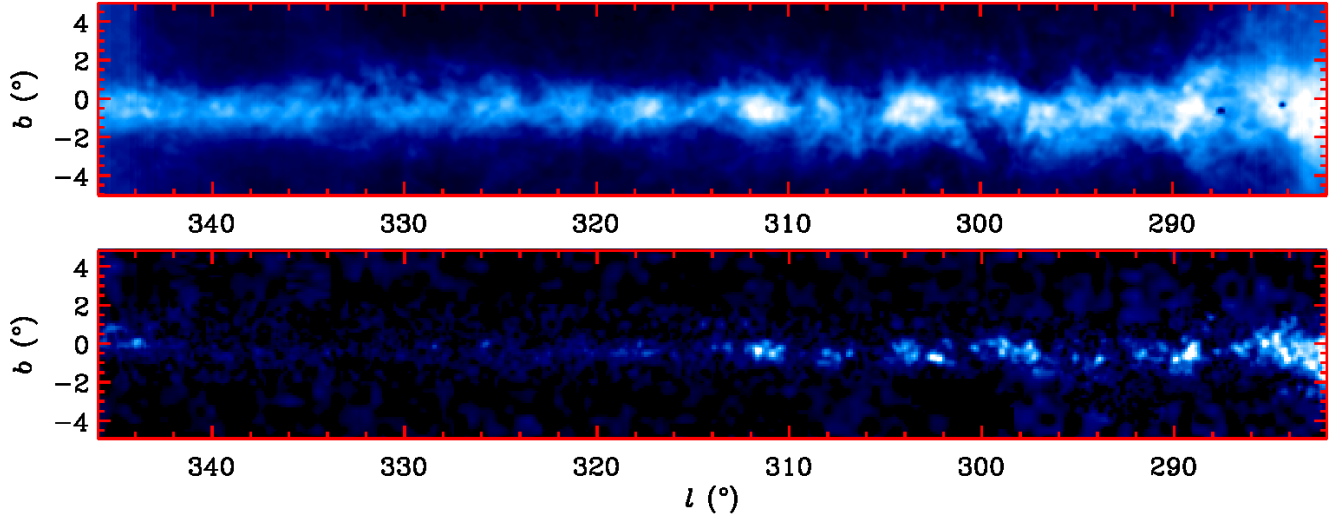
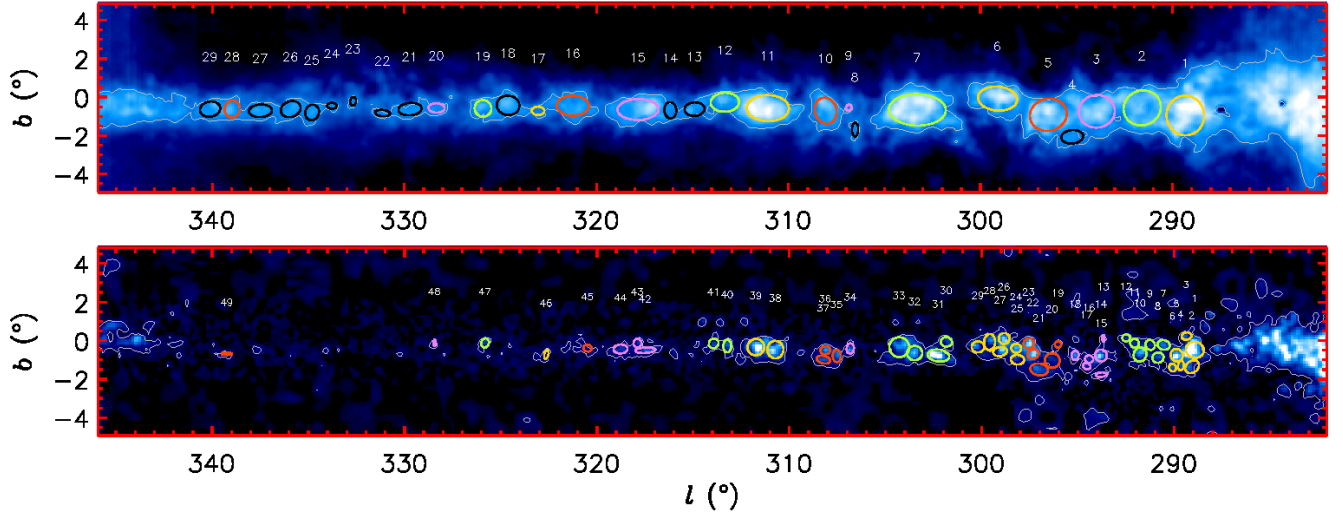


Figure 1. (l, v_{LSR}) diagrams with the locations of the outer Carina arm. The outer Carina arm traces obtained by Paper I are overlaid with a zigzagging solid line in each panel. *Top:* b -integrated local peak intensities in HI ($= \sum_{b=-10^\circ}^{b=+30^\circ} T_{b,\text{max}}(l, b, v_{\text{LSR}})$) from the LAB HI data used in Paper I. Contour levels are 20, 40, 60, and 80 K. *Middle:* b -averaged HI intensities from $b = -2^\circ$ to $+1^\circ$ from the HI4PI data. Contour levels are 30, 40, 50, 60, 70, and 80 K. *Bottom:* Similar to the middle panel, but showing the CfA CO data. Contour levels are 0.1 and 0.5 K. All three images are displayed on a square-root scale. Two thick dotted lines spaced approximately 25 km s^{-1} apart indicate the velocity range from which the v -integrated maps in Figure 2(a) are obtained. Two thin dotted lines at $l > 332^\circ$ aid in locating an interval of $\pm 8 \text{ km s}^{-1}$ from the solid line mentioned in Sections 3.1.2. A horizon (black or white) line is included to indicate where $v_{\text{LSR}} = 0 \text{ km s}^{-1}$.

(a) v -integrated H I and CO maps of the outer Carina arm

(b) H I and CO maps of the outer Carina arm with cloud identification

Figure 2. (l, b) maps of the outer Carina arm in H I and CO. These maps are obtained by integrating spectra within a range of about 25 km s^{-1} centered around the outer Carina arm traces in Figure 1. The top panels show a v -integrated HI4PI H I map on a square-root scale, with a range of 100 to 2600 K km s^{-1} . The bottom panels show v -integrated CfA CO map on the same scale, with a range of 0 to 20 K km s^{-1} . Figure 2(b) is the same as Figure 2(a), but with contours and labels indicating H I and CO clouds identified in this study. A contour in the top panel indicates the lowest H I level of 1210 K km s^{-1} described in Section 3.1.1, while a contour in the bottom panel is drawn at the lowest CO level of 2.5 K km s^{-1} described in Section 3.1.1. Best-fit ellipses are drawn to aid in locating the H I clouds in Figure 2(b), and, in its bottom panel, the colors of circles are the same as those of associated H I clouds. The colors of the circles indicate whether they are matched with MCs, and the floating numbers correspond to those assigned to the H I clouds or MCs. Three H I clouds, H4, H9, and H22, and one MC of M34 are excluded from further analysis and discussion (see Section 3.1.1 for details).

efficiently and accurately extract the velocity component(s) of the HI cloud, we obtain an area-averaged velocity profile from a specific region within the cloud. The cloud area is determined using the CLUMPFIND process, which clips at the minimum velocity-integrated intensity, 1210 K km s^{-1} . We then fit the area-averaged velocity profile to a Gaussian Mixture Model (GMM) using the `sklearn.mixture.GaussianMixture` function in python.² This algorithm, which is an unsupervised learning algorithm for clustering, is advantageous in that it does not require an initial setting of the number of Gaussian components and their parameters. In situations where a profile exhibits complexity, the resulting best-fit values can differ based on the value of the “*random_state*” parameter, which controls the random seed for initialization. To mitigate this, we performed 100 iterations with *random_state* values ranging from 0 to 99, and utilized a value of *tol* ($= 1e-5$; the convergence threshold) larger than the default threshold, as determined by manual inspection. The average parameters and their standard deviations were computed.³ Smaller standard deviation values suggest that the decomposition results converge to a specific case with greater clarity. Conversely, larger standard deviation values indicate that the profile for a given velocity range may have multiple possible solutions.

The kinematic selection of the decomposed Gaussian components is based on their central velocities, which are compared to the mean velocity of the outer Carina arm traces with the longitude range of each cloud. We accept Gaussian components that fall within a velocity range of $\pm 12.5 \text{ km s}^{-1}$ for $l \leq 332^\circ$ and $\pm 8 \text{ km s}^{-1}$ for $l > 332^\circ$. The narrower velocity range for the latter is chosen because the corresponding HI emission features, as seen in the position-velocity diagram (see Figure 1), are distributed over a relatively narrower velocity range than in the former case.

On the other hand, the CO emission features appear to be relatively isolated and exhibit almost no extended diffuse emission feature. We performed a decomposition process of the velocity component(s) for the CO data, similar to that described above for the HI data, but with the additional criterion that only those Gaussian components with peaks that are $3 \times T_{\text{rms}}$ or higher were

² An example of a one-dimensional GMM can be found at https://www.astroml.org/book_figures/chapter4/fig_GMM_1D.html.

³ Out of the identified HI clouds, convergence issues were encountered in some iterations of the GMM fitting for eight of them. Consequently, statistical values were derived from the iterations that achieved successful convergence and those that did not were excluded from the calculation.

retained. T_{rms} is the noise level, which was determined from regions where no astronomical signal is present.

3.2. Derivation of Physical Parameters

3.2.1. Position and Size

The central position (l_c, b_c) of each cloud is determined by fitting a best-fit ellipse to Galactic coordinates within the clumpfind-result area using the IDL procedure MPFITELLIPSE (Markwardt 2009). This fitting also calculates the semi-major/minor axes (r_{major} and r_{minor} , respectively). For HI clouds, a position angle (PA) is a free-fitting parameter, whereas it is set to be 0 for MCs. The presented PA in this paper is a counter-clockwise rotation angle measured from the $+b$ -axis. The best-fit ellipses represent about 50% of the clumpfind-result area on average. In estimating other parameters, such as column density and mass, we use a geometrical mean radius (r_{geo}), which is defined as the radius of an imaginary circle with the same clumpfind-result area (A) as given by Equation 1.

$$r_{\text{geo}} = \sqrt{A/\pi}. \quad (1)$$

3.2.2. Central Velocity and Velocity Dispersion

The central velocity (v_c) and velocity dispersion (σ_v) of each cloud are estimated through Gaussian decomposition of the area-averaged velocity ($\bar{T}(v)$) profile, as described in Section 3.1.2. These parameters are intensity-weighted and computed as follows:

$$v_c = \frac{\sum_v v \mathcal{G}(v) dv}{\sum_v \mathcal{G}(v) dv}, \quad (2)$$

$$\sigma_v = \sqrt{\frac{\sum_v (v - v_c)^2 \mathcal{G}(v) dv}{\sum_v \mathcal{G}(v) dv}}, \quad (3)$$

where $\mathcal{G}(v) (= \sum_{\text{clouds}} \bar{T}(v)_{\text{Gauss}})$ represents the sum of Gaussian components that are identified as being associated with each cloud, also explained in Section 3.1.2.

3.2.3. Distance

Based on the derived central velocity, we calculate the kinematic distance to each cloud by employing the flat Galactic rotation model of Reid & Dame (2016), which updates the model presented in Reid et al. (2014). The model provides the Sun’s distance to the Galactic center as $R_0 = 8.34 \text{ kpc}$ and the Sun’s rotational speed as $\Theta_0 = 240 \text{ km s}^{-1}$.

3.2.4. Mass and Surface Density

The mass of each HI cloud is determined using the expression:

$$M_{\text{HI}} = N_{\text{HI}} \times \pi r_{\text{geo,HI}}^2 \times m_{\text{H}} \times 1.36, \quad (4)$$

where $r_{\text{geo,H I}}$ is the geometrical mean radius of the H I cloud as defined earlier, m_{H} is the mass of a hydrogen atom, and 1.36 is mean atomic mass per H atom (Allen 1973).

The H I column density (N_{HI}) is calculated under the assumption of a constant spin temperature (T_{s}), following Levine et al. (2006), where T_{s} is assumed to be 155 K. The calculation is based on the area-averaged velocity profile, from which the portion associated with a given cloud is extracted. The equation for N_{HI} is given by:

$$N_{\text{HI}} = 1.82 \times 10^{18} \sum_v -T_{\text{s}} \ln \left(1 - \frac{\mathcal{G}(v)}{T_{\text{s}}} \right) dv. \quad (5)$$

Similarly, the mass of each MC (M_{H_2}), which represents the total mass of molecular hydrogen, is calculated using the following equation:

$$M_{\text{H}_2} = X_{\text{CO}} \times \sum_v \mathcal{G}(v) dv \times \pi r_{\text{geo,CO}}^2 \times m_{\text{H}} \times 2.72, \quad (6)$$

where X_{CO} is the CO-to-H₂ conversion factor of 2×10^{20} (K km s⁻¹)⁻¹ cm⁻² (Bolatto et al. 2013), and 2.72 is the mean atomic mass per H₂ molecule.

Although CO is commonly used as a tracer of molecular hydrogen gas, it is known that molecular gas exists without being detected by CO lines. This phenomenon has been observed (e.g., Grenier et al. 2005; Abdo et al. 2010; Planck Collaboration et al. 2011a,b) and theoretically predicted (e.g., van Dishoeck & Black 1988; Wolfire et al. 2010). To address this issue, alternative tracers such as OH, HCO⁺, and C⁺ lines have been utilized in many observational studies (e.g., Liszt & Lucas 1996; Lucas & Liszt 1996; Tang et al. 2017; Park et al. 2018). Studies by Pineda et al. (2013) have revealed the existence of CO-dark molecular gas, which is warm and diffuse, extends over a wider range of Galactocentric distance (R_{GC}) than the cold and dense molecular gas traced by ¹²CO and ¹³CO. The contribution of CO-dark molecular gas increases with increasing R_{GC} , resulting in an increase in the X_{CO} conversion factor as well. From the relation between X_{CO} and R_{GC} presented in Figure 20 of Pineda et al. (2013), it is evident that X_{CO} increases by a factor of approximately 1.5 to 2.5 in the R_{GC} range of (9, 11) kpc. For this study, we have adopted the conventional X_{CO} , which means that the resulting M_{H_2} values may represent a lower limit of the actual total molecular cloud mass.

3.2.5. Basic Properties

Tables 1 and 2 provide the physical parameters of the 29 H I clouds and 49 MCs identified in this study. The geometrical mean radii of 26 H I clouds, except H4, H9, and H22, range from 74 pc to 318 pc with a mean value

of 187 pc. The H I cloud mass ranges from $4.2 \times 10^5 M_{\odot}$ to $2.0 \times 10^7 M_{\odot}$, with most clouds (23 of 26) being more massive than $10^6 M_{\odot}$. The mean H I cloud mass is calculated to be $5.9 \times 10^6 M_{\odot}$. According to the classification of Elmegreen & Elmegreen (1987, hereafter, EE87), clouds with a mass greater than $\sim 10^6 M_{\odot}$ are referred to as H I *superclouds*, and most clouds in this study can be classified as such.

It is noteworthy that all CO-bright H I clouds observed in this study have masses greater than $1 \times 10^6 M_{\odot}$, with the majority exceeding $5 \times 10^6 M_{\odot}$. These clouds also exhibit H I surface densities of $\Sigma_{\text{HI}} \gtrsim 34 M_{\odot} \text{pc}^{-2}$, while some CO-dark H I clouds have H I surface densities ranging from $34 M_{\odot} \text{pc}^{-2}$ to $47 M_{\odot} \text{pc}^{-2}$. In addition, with respect to the surface density of total gas (see Equation 13), the majority of CO-bright H I clouds have values of $\Sigma_{\text{HI+H}_2} \gtrsim 50 M_{\odot} \text{pc}^{-2}$, while the minimum value for the H I clouds in this study is $21.3 M_{\odot} \text{pc}^{-2}$.

Observational studies of extragalaxies and the Milky Way suggest that a minimum H I surface density of $\sim 10 M_{\odot} \text{pc}^{-2}$ at solar metallicity is required for H₂ formation (e.g., Wong & Blitz 2002; Bigiel et al. 2008; Lee et al. 2012b, 2015). The Analytical study by Krumholz et al. (2009) has shown that H₂ formation is closely related to metallicity and total gas surface density. Based on the Galactic metallicity gradient shown in (Pedicelli et al. 2009) and the fact that our H I clouds are located at $R_{\text{GC}} \sim 9\text{--}11$ kpc, a rough estimate suggests that the metallicity has decreased to about 0.8 times the solar value, while the most extreme case indicated in their Figure 3 suggests a value of about 0.3 times the solar value. For the 11 out of 26 H I clouds in our sample that do not show detectable CO emission according to our criteria, the absence of CO may be due to the need for higher H I surface densities resulting from their lower metallicity, although the possibility of CO emission with column densities below our detection limit cannot be entirely excluded.

However, it should be noted that the previous studies of the minimum H I surface density required for H₂ formation were derived from pixel-to-pixel analysis, while this study is based on the total area of each cloud. Therefore, a direct comparison between the two values should be made with caution.

The average geometrical mean radius of 48 MCs, excluding M34, is 70 pc, and their M_{H_2} ranges from $3.6 \times 10^4 M_{\odot}$ to $3.7 \times 10^6 M_{\odot}$, with a mean value of $6.0 \times 10^5 M_{\odot}$. Of the 48 MCs, 41 have M_{H_2} values that

Table 1. H I Superclouds in the Carina Arm ($288^\circ \lesssim l \lesssim 340^\circ$)

# _{H I}	l_c^*	b_c^*	r_{major}^*	r_{minor}^*	PA [*]	r_{geo}	v_c^\dagger	σ_v^\dagger	d	R_{GC}	r_{geo}	$\Sigma_{\text{H I}}^\ddagger$	$M_{\text{H I}}^\ddagger$
(1)	($^\circ$)	($^\circ$)	($^\circ$)	($^\circ$)	($^\circ$)	($^\circ$)	(km s^{-1})	(km s^{-1})	(kpc)	(kpc)	(pc)	($\text{M}_\odot \text{pc}^{-2}$)	(M_\odot)
(1)	(2)	(3)	(4)	(5)	(6)	(7)	(8)	(9)	(10)	(11)	(12)	(13)	(14)
H1	289.34 (0.01)	-0.95 (0.01)	1.03 (0.01)	0.98 (0.01)	8 (9)	1.43	+19.3 (2.4)	8.2 (1.2)	7.4	9.1	184	67.4 (14.5)	7.2e+6 (1.6e+6)
H2	291.58 (0.01)	-0.56 (0.01)	0.98 (0.01)	0.90 (0.01)	111 (10)	1.30	+24.9 (2.3)	8.4 (1.3)	8.3	9.4	189	54.0 (9.2)	6.0e+6 (1.0e+6)
H3	293.95 (0.01)	-0.74 (0.01)	0.94 (0.01)	0.85 (0.01)	96 (7)	1.27	+24.7 (1.7)	8.0 (1.0)	8.9	9.4	197	58.4 (9.7)	7.1e+6 (1.2e+6)
H4	295.23 (0.02)	-2.06 (0.01)	0.57 (0.01)	0.35 (0.01)	95 (3)	0.62	+22.0 (2.1)	8.2 (1.2)	8.9	9.3	96	42.1 (7.7)	1.2e+6 (2.2e+5)
H5	296.47 (0.01)	-0.92 (0.01)	0.97 (0.01)	0.83 (0.01)	104 (3)	1.29	+22.3 (1.6)	8.6 (0.9)	9.3	9.3	209	64.8 (8.7)	8.9e+6 (1.2e+6)
H6	299.11 (0.02)	-0.08 (0.01)	1.02 (0.01)	0.62 (0.01)	85 (1)	1.18	+24.4 (2.4)	8.4 (1.1)	10.0	9.4	205	53.8 (8.7)	7.1e+6 (1.1e+6)
H7	303.29 (0.02)	-0.66 (0.01)	1.49 (0.01)	0.82 (0.01)	89 (1)	1.60	+29.4 (2.1)	8.0 (1.1)	11.4	9.8	318	61.9 (11.9)	2.0e+7 (3.8e+6)
H8	306.53 (0.01)	-1.68 (0.02)	0.36 (0.02)	0.16 (0.01)	179 (3)	0.34	+33.6 (1.3)	8.2 (1.0)	12.5	10.1	74	44.7 (6.2)	7.7e+5 (1.1e+5)
H9	306.86 (0.01)	-0.55 (0.01)	0.17 (0.01)	0.14 (0.01)	163 (27)	0.23	+34.2 (2.1)	9.1 (1.2)	12.6	10.1	50	44.5 (8.2)	3.4e+5 (6.2e+4)
H10	308.06 (0.01)	-0.71 (0.01)	0.69 (0.01)	0.56 (0.01)	15 (5)	0.91	+31.7 (2.8)	7.3 (1.2)	12.7	10.0	202	42.2 (10.5)	5.4e+6 (1.3e+6)
H11	311.07 (0.02)	-0.57 (0.01)	1.10 (0.01)	0.68 (0.01)	89 (1)	1.28	+33.1 (2.9)	8.6 (1.3)	13.5	10.2	303	61.2 (15.3)	1.8e+7 (4.5e+6)
H12	313.31 (0.02)	-0.27 (0.01)	0.74 (0.01)	0.49 (0.01)	92 (2)	0.80	+32.8 (2.1)	12.5 (5.9)	14.0	10.2	195	46.8 (9.9)	5.6e+6 (1.2e+6)
H13	314.89 (0.02)	-0.62 (0.01)	0.52 (0.02)	0.35 (0.01)	94 (4)	0.57	+36.2 (2.0)	8.6 (1.2)	14.7	10.6	145	47.3 (9.4)	3.1e+6 (6.2e+5)
H14	316.15 (0.01)	-0.68 (0.02)	0.42 (0.02)	0.31 (0.01)	5 (5)	0.46	+34.8 (1.9)	8.8 (1.5)	14.8	10.5	120	43.8 (9.4)	2.0e+6 (4.3e+5)
H15	317.83 (0.02)	-0.64 (0.01)	1.07 (0.01)	0.54 (0.01)	91 (1)	1.13	+35.8 (3.0)	8.0 (1.3)	15.3	10.7	301	51.1 (11.8)	1.5e+7 (3.5e+6)
H16	321.23 (0.02)	-0.44 (0.01)	0.84 (0.01)	0.52 (0.01)	89 (2)	0.94	+29.1 (2.5)	10.0 (3.4)	15.4	10.3	251	47.4 (9.1)	9.4e+6 (1.8e+6)
H17	323.04 (0.02)	-0.71 (0.01)	0.33 (0.01)	0.22 (0.01)	89 (6)	0.36	+24.7 (1.7)	7.5 (0.9)	15.4	10.0	97	40.0 (7.1)	1.2e+6 (2.1e+5)
H18	324.60 (0.01)	-0.43 (0.01)	0.59 (0.01)	0.50 (0.01)	83 (7)	0.77	+25.9 (2.2)	8.3 (1.3)	15.8	10.2	213	46.6 (11.0)	6.6e+6 (1.6e+6)
H19	325.91 (0.01)	-0.58 (0.01)	0.44 (0.01)	0.43 (0.01)	66 (131)	0.63	+27.7 (2.4)	8.1 (1.4)	16.3	10.5	178	45.2 (10.2)	4.5e+6 (1.0e+6)
H20	328.32 (0.02)	-0.56 (0.01)	0.42 (0.01)	0.24 (0.01)	88 (3)	0.47	+32.0 (1.9)	7.5 (0.9)	17.4	11.2	142	39.1 (7.9)	2.5e+6 (5.1e+5)
H21	329.71 (0.02)	-0.62 (0.01)	0.61 (0.02)	0.32 (0.01)	95 (2)	0.60	+30.9 (1.6)	10.2 (3.0)	17.5	11.2	182	42.7 (7.2)	4.5e+6 (7.6e+5)
H22	331.13 (0.03)	-0.83 (0.01)	0.39 (0.02)	0.16 (0.01)	85 (4)	0.34	+29.9 (2.3)	10.1 (3.0)	17.8	11.2	105	44.4 (10.9)	1.5e+6 (3.7e+5)
H23	332.67 (0.01)	-0.21 (0.02)	0.22 (0.01)	0.15 (0.01)	172 (9)	0.27	+20.7 (2.1)	6.7 (1.1)	16.9	10.3	80	21.3 (5.2)	4.2e+5 (1.0e+5)
H24	333.77 (0.02)	-0.45 (0.01)	0.25 (0.01)	0.16 (0.01)	87 (8)	0.29	+20.6 (2.5)	7.4 (2.8)	17.1	10.3	86	26.7 (7.9)	6.3e+5 (1.9e+5)
H25	334.81 (0.01)	-0.79 (0.02)	0.41 (0.01)	0.35 (0.01)	158 (12)	0.54	+19.1 (1.8)	6.1 (0.9)	17.1	10.2	162	29.2 (7.2)	2.4e+6 (5.9e+5)
H26	335.92 (0.02)	-0.62 (0.01)	0.53 (0.01)	0.40 (0.01)	109 (6)	0.66	+19.5 (1.2)	6.1 (1.0)	17.4	10.4	201	28.7 (6.4)	3.6e+6 (8.1e+5)
H27	337.49 (0.02)	-0.71 (0.01)	0.60 (0.01)	0.33 (0.01)	93 (2)	0.66	+20.6 (2.2)	6.3 (1.3)	17.9	10.7	206	27.6 (8.8)	3.7e+6 (1.2e+6)
H28	338.96 (0.01)	-0.62 (0.01)	0.44 (0.01)	0.40 (0.01)	169 (12)	0.60	+21.8 (1.6)	6.0 (1.3)	18.5	11.1	193	34.1 (9.3)	4.0e+6 (1.1e+6)
H29	340.12 (0.02)	-0.62 (0.01)	0.53 (0.01)	0.39 (0.01)	100 (4)	0.67	+22.3 (1.7)	5.7 (0.5)	18.9	11.4	220	33.0 (6.2)	5.0e+6 (9.4e+5)

NOTE—(1) Number assigned to a H I cloud; (2–3) central position in Galactic coordinates; (4–6) semi-major/minor axes and position angle (PA) of a best-fit ellipse; (7) angular geometrical mean radius; (8) intensity-weighted mean LSR velocity; (9) intensity-weighted velocity dispersion; (10) Heliocentric distance; (11) Galactocentric distance; (12) linear geometrical mean radius; (13) surface density; (14) H I cloud mass.

* These parameters were derived by an ellipse-fitting. The value in parentheses is 1σ uncertainty of each derived ellipse parameter.

† The standard deviation of the outputs from 100 iterations.

‡ The given uncertainty considers only that of the surface density (relevant to integral of decomposed Gaussian components), not including that of distance.

equal or exceed 10^5 M_\odot , which implies that either giant molecular clouds or groups of MCs, namely, molecular cloud complexes.

In terms of H I clouds, we investigated the relationship between R_{GC} and mass or radius using the Spearman's rank correlation test, which examines if two variables are monotonically related. We found a weak negative correlation between R_{GC} and the H I mass of H I clouds (Spearman's correlation coefficient (ρ) = -0.36 and p-value = 0.071). This means that as R_{GC} increases, the H I mass tends to decrease. However, the correlation is not statistically significant, so it is unclear whether the two variables have a real relationship. On the other

hand, we found that there is a strong negative correlation between R_{GC} and H_2 mass assigned to the corresponding H I clouds (ρ = -0.52 and p-value = 0.048). This means that as R_{GC} increases, the H_2 mass tends to decrease. The p-value is very small, so the correlation is statistically significant. Finally, we found that there is no correlation between R_{GC} and r_{geo} of the H I clouds (ρ = -0.085 and p-value = 0.68). This means that there is no clear relationship between the two variables.

3.3. Spatial Distribution of H I Superclouds

Most of the identified H I superclouds and MCs are below $b = 0^\circ$. The mean deviation from $b = 0^\circ$ is $\Delta b \simeq -0.6^\circ$, corresponding to a linear distance of

Table 2. Molecular Clouds in the Carina Arm ($288^\circ \lesssim l \lesssim 340^\circ$)

#CO	#HI	l_c^*	b_c^*	r_{major}^*	r_{minor}^*	PA [*]	r_{geo}	v_c^\dagger	σ_v^\dagger	d	R_{GC}	r_{geo}	$\Sigma_{\text{H}_2}^\ddagger$	$M_{\text{H}_2}^\ddagger$
(1)	(2)	($^\circ$)	($^\circ$)	($^\circ$)	($^\circ$)	($^\circ$)	($^\circ$)	(km s^{-1})	(km s^{-1})	(kpc)	(kpc)	(pc)	($\text{M}_\odot \text{pc}^{-2}$)	(M_\odot)
M1	H1	288.93 (0.02)	-0.48 (0.02)	0.47 (0.02)	0.42 (0.02)	29 (29)	0.62	+21.1 (0.3)	7.2 (0.5)	7.4	9.2	80	80.9 (1.7)	1.6e+6 (3.3e+4)
M2	H1	289.07 (0.04)	-1.36 (0.03)	0.39 (0.04)	0.29 (0.03)	37 (40)	0.37	+21.4 (0.7)	6.9 (0.9)	7.5	9.2	49	28.8 (1.7)	2.2e+5 (1.3e+4)
M3	H1	289.37 (0.02)	+0.24 (0.02)	0.26 (0.02)	0.19 (0.01)	174 (10)	0.32	+19.8 (1.6)	4.3 (1.8)	7.4	9.1	42	19.0 (4.5)	1.0e+5 (2.4e+4)
M4	H1	289.66 (0.02)	-1.29 (0.03)	0.26 (0.02)	0.15 (0.01)	100 (13)	0.28	+19.3 (0.6)	9.5 (0.5)	7.4	9.1	36	41.8 (1.9)	1.7e+5 (7.8e+3)
M5	H1	289.87 (0.02)	-0.76 (0.02)	0.33 (0.02)	0.31 (0.02)	126 (36)	0.43	+17.8 (1.8)	6.6 (0.8)	7.3	9.0	55	38.9 (7.2)	3.7e+5 (6.8e+4)
M6	H1	290.09 (0.02)	-1.40 (0.02)	0.21 (0.02)	0.17 (0.02)	79 (25)	0.28	+15.2 (1.6)	6.1 (1.4)	7.2	8.9	35	24.4 (3.1)	9.6e+4 (1.2e+4)
M7	H2	290.55 (0.03)	-0.23 (0.02)	0.33 (0.02)	0.25 (0.02)	97 (32)	0.40	+22.9 (1.5)	7.7 (0.9)	7.9	9.3	55	26.8 (3.3)	2.5e+5 (3.0e+4)
M8	H2	290.85 (0.02)	-0.88 (0.02)	0.29 (0.02)	0.27 (0.01)	41 (***)	0.39	+22.4 (2.2)	7.7 (1.6)	8.0	9.3	55	19.7 (3.1)	1.9e+5 (3.0e+4)
M9	H2	291.25 (0.02)	-0.22 (0.03)	0.27 (0.02)	0.24 (0.02)	155 (21)	0.32	+20.9 (1.9)	7.5 (1.9)	7.9	9.2	43	16.0 (3.5)	9.5e+4 (2.0e+4)
M10	H2	291.78 (0.02)	-0.72 (0.03)	0.37 (0.02)	0.33 (0.01)	27 (60)	0.46	+22.2 (0.3)	8.0 (0.3)	8.2	9.3	66	38.8 (0.8)	5.3e+5 (1.1e+4)
M11	H2	292.07 (0.02)	-0.14 (0.02)	0.23 (0.02)	0.22 (0.02)	110 (39)	0.33	+24.4 (<0.1)	5.5 (<0.1)	8.4	9.4	48	18.0 (<0.1)	1.3e+5 (1.0e+2)
M12	H2	292.50 (0.02)	+0.14 (0.02)	0.21 (0.02)	0.18 (0.01)	77 (18)	0.27	+19.7 (0.5)	2.7 (0.5)	8.1	9.1	39	13.0 (1.0)	6.1e+4 (4.4e+3)
M13	H3	293.69 (0.02)	+0.12 (0.03)	0.17 (0.04)	0.06 (0.03)	68 (28)	0.17	+25.5 (0.1)	2.7 (<0.1)	8.9	9.4	27	15.9 (0.2)	3.6e+4 (5.2e+2)
M14	H3	293.81 (0.02)	-0.77 (0.03)	0.31 (0.02)	0.30 (0.02)	82 (52)	0.39	+29.5 (0.2)	5.4 (0.2)	9.2	9.6	63	41.1 (1.7)	5.1e+5 (2.1e+4)
M15	H3	293.81 (0.04)	-1.77 (0.02)	0.28 (0.04)	0.12 (0.02)	23 (163)	0.24	+21.4 (0.1)	2.6 (0.1)	8.6	9.2	37	16.2 (0.2)	6.9e+4 (1.0e+3)
M16	H3	294.43 (0.02)	-0.96 (0.03)	0.22 (0.03)	0.19 (0.03)	180 (14)	0.29	+28.6 (0.9)	9.9 (1.6)	9.3	9.6	47	27.0 (3.0)	1.9e+5 (2.1e+4)
M17	H3	294.55 (0.03)	-1.33 (0.02)	0.21 (0.02)	0.16 (0.02)	113 (55)	0.26	+23.3 (<0.1)	3.0 (<0.1)	8.9	9.3	41	17.5 (0.2)	9.2e+4 (1.2e+3)
M18	H3	295.15 (0.02)	-0.77 (0.02)	0.24 (0.02)	0.19 (0.01)	106 (19)	0.31	+24.3 (2.3)	7.7 (1.5)	9.1	9.4	49	29.1 (5.6)	2.2e+5 (4.2e+4)
M19	H5	296.04 (0.03)	-0.20 (0.03)	0.17 (0.02)	0.16 (0.04)	83 (6)	0.21	+15.4 (1.6)	3.9 (0.9)	8.6	9.0	32	15.8 (1.6)	5.0e+4 (5.0e+3)
M20	H5	296.34 (0.03)	-1.03 (0.03)	0.39 (0.03)	0.37 (0.03)	80 (145)	0.49	+21.9 (2.2)	6.5 (2.2)	9.2	9.3	78	18.3 (<0.1)	3.5e+5 (5.8e-1)
M21	H5	297.02 (0.02)	-1.50 (0.02)	0.47 (0.02)	0.31 (0.01)	119 (***)	0.54	+21.7 (<0.1)	5.3 (<0.1)	9.3	9.3	88	23.5 (<0.1)	5.7e+5 (9.8e+1)
M22	H5	297.34 (0.02)	-0.70 (0.02)	0.30 (0.02)	0.25 (0.02)	176 (9)	0.40	+23.4 (0.3)	7.0 (0.2)	9.5	9.4	66	53.8 (1.2)	7.4e+5 (1.6e+4)
M23	H5	297.56 (0.02)	-0.14 (0.02)	0.28 (0.02)	0.26 (0.01)	98 (8)	0.40	+19.5 (0.2)	5.2 (0.1)	9.3	9.2	65	56.3 (1.3)	7.4e+5 (1.7e+4)
M24	H6	298.15 (0.03)	-0.99 (0.02)	0.34 (0.02)	0.25 (0.02)	132 (***)	0.38	+23.0 (0.1)	6.0 (0.1)	9.7	9.4	64	21.2 (0.1)	2.5e+5 (1.5e+3)
M25	H6	298.22 (0.02)	-0.40 (0.02)	0.26 (0.02)	0.23 (0.02)	84 (31)	0.36	+24.5 (<0.1)	7.8 (<0.1)	9.8	9.4	62	47.9 (<0.1)	6.4e+5 (1.7e+2)
M26	H6	298.84 (0.02)	+0.11 (0.02)	0.28 (0.02)	0.28 (0.02)	52 (***)	0.41	+23.8 (0.2)	5.5 (0.2)	9.9	9.4	70	45.3 (0.9)	7.0e+5 (1.4e+4)
M27	H6	299.05 (0.03)	-0.57 (0.02)	0.36 (0.03)	0.24 (0.02)	90 (63)	0.41	+25.0 (0.2)	6.7 (0.1)	10.1	9.5	71	40.1 (0.9)	6.4e+5 (1.4e+4)
M28	H6	299.60 (0.02)	-0.08 (0.03)	0.42 (0.02)	0.29 (0.01)	83 (5)	0.46	+23.3 (<0.1)	7.7 (<0.1)	10.1	9.4	81	28.4 (<0.1)	5.8e+5 (8.1e+2)
M29	H6	300.20 (0.03)	-0.33 (0.03)	0.33 (0.02)	0.29 (0.02)	86 (16)	0.42	+30.6 (<0.1)	4.9 (<0.1)	10.8	9.8	79	28.7 (<0.1)	5.6e+5 (2.8e+2)
M30	H7	301.84 (0.02)	-0.07 (0.02)	0.30 (0.02)	0.24 (0.02)	174 (13)	0.37	+23.9 (0.1)	4.0 (0.1)	10.6	9.4	69	24.0 (0.5)	3.4e+5 (7.3e+3)
M31	H7	302.26 (0.03)	-0.78 (0.02)	0.56 (0.02)	0.31 (0.01)	77 (7)	0.58	+30.5 (<0.1)	4.7 (<0.1)	11.3	9.8	115	47.7 (0.4)	2.0e+6 (1.8e+4)
M32	H7	303.49 (0.02)	-0.65 (0.02)	0.39 (0.02)	0.37 (0.02)	93 (18)	0.54	+27.9 (<0.1)	6.0 (<0.1)	11.3	9.7	106	37.7 (<0.1)	1.3e+6 (1.4e+3)
M33	H7	304.29 (0.03)	-0.34 (0.03)	0.52 (0.02)	0.51 (0.02)	2 (8)	0.67	+29.5 (0.1)	5.6 (0.2)	11.6	9.8	136	31.9 (1.0)	1.9e+6 (6.1e+4)
M34	H9	306.84 (0.02)	-0.41 (0.02)	0.27 (0.02)	0.19 (0.01)	114 (37)	0.32	+24.8 (0.1)	3.2 (0.1)	11.9	9.6	67	26.2 (0.6)	3.7e+5 (8.4e+3)
M35	H10	307.54 (0.02)	-0.79 (0.02)	0.33 (0.02)	0.21 (0.01)	0 (32)	0.39	+32.7 (0.1)	3.8 (<0.1)	12.7	10.1	86	27.9 (0.4)	6.4e+5 (9.0e+3)
M36	H10	308.14 (0.02)	-0.50 (0.02)	0.26 (0.02)	0.22 (0.02)	135 (62)	0.35	+32.1 (0.1)	6.6 (<0.1)	12.7	10.0	77	31.8 (0.2)	5.9e+5 (4.1e+3)
M37	H10	308.23 (0.03)	-0.99 (0.02)	0.36 (0.03)	0.20 (0.02)	0 (10)	0.38	+37.2 (0.3)	4.0 (0.9)	13.2	10.4	87	19.7 (3.5)	4.7e+5 (8.4e+4)
M38	H11	310.73 (0.02)	-0.47 (0.02)	0.45 (0.02)	0.42 (0.02)	92 (7)	0.63	+28.2 (0.7)	7.9 (0.6)	13.0	9.9	142	41.9 (4.8)	2.7e+6 (3.1e+5)
M39	H11	311.74 (0.02)	-0.34 (0.02)	0.44 (0.02)	0.42 (0.01)	171 (***)	0.62	+28.6 (0.5)	9.2 (1.2)	13.3	9.9	144	57.5 (4.4)	3.7e+6 (2.8e+5)
M40	H12	313.23 (0.02)	-0.28 (0.03)	0.33 (0.02)	0.21 (0.01)	93 (2)	0.37	+43.0 (<0.1)	3.9 (<0.1)	14.9	11.0	95	29.3 (0.2)	8.4e+5 (5.1e+3)
M41	H12	313.93 (0.03)	-0.14 (0.03)	0.26 (0.03)	0.24 (0.02)	77 (149)	0.32	+32.6 (<0.1)	6.0 (<0.1)	14.1	10.3	80	21.0 (0.1)	4.2e+5 (2.5e+3)
M42	H15	317.49 (0.04)	-0.51 (0.01)	0.53 (0.04)	0.14 (0.01)	90 (8)	0.40	+30.1 (0.2)	5.8 (0.2)	14.7	10.2	102	22.3 (1.2)	7.3e+5 (4.1e+4)
M43	H15	317.90 (0.03)	-0.13 (0.03)	0.23 (0.03)	0.21 (0.02)	180 (14)	0.27	+23.7 (4.3)	8.0 (1.9)	14.2	9.8	68	34.4 (11)	5.0e+5 (1.7e+5)
M44	H15	318.78 (0.03)	-0.44 (0.02)	0.37 (0.02)	0.23 (0.01)	163 (38)	0.39	+35.1 (<0.1)	4.1 (<0.1)	15.5	10.7	104	19.4 (0.3)	6.6e+5 (8.6e+3)
M45 [§]	H16	320.49 (0.04)	-0.39 (0.04)	0.22 (0.03)	0.18 (0.05)	167 (19)	0.27	+22.7 (1.1)	4.8 (2.2)	14.7	9.8	70	17.4 (6.7)	2.7e+5 (1.0e+5)
M46 [§]	H17	322.63 (0.02)	-0.72 (0.04)	0.22 (0.03)	0.10 (0.02)	89 (62)	0.21	+19.0 (0.9)	6.2 (0.5)	14.8	9.6	55	20.2 (2.2)	1.9e+5 (2.1e+4)
M47 [§]	H19	325.81 (0.02)	-0.12 (0.03)	0.24 (0.02)	0.20 (0.02)	86 (14)	0.29	+29.2 (0.8)	5.0 (1.0)	16.4	10.6	83	20.8 (2.1)	4.5e+5 (4.4e+4)
M48 [§]	H20	328.44 (0.02)	-0.12 (0.03)	0.17 (0.04)	0.06 (0.03)	175 (16)	0.17	+31.0 (<0.1)	3.2 (<0.1)	17.3	11.0	52	23.7 (<0.1)	2.0e+5 (8.2e+0)
M49	H28	339.23 (0.06)	-0.69 (0.02)	0.28 (0.08)	0.06 (0.04)	95 (7)	0.17	+23.4 (1.4)	7.5 (1.2)	18.9	11.5	57	17.6 (2.2)	1.8e+5 (2.2e+4)

NOTE— (1) Number assigned to a MC; (2) Number of associated HI cloud; (3–4) central position in Galactic coordinates; (5–7) semi-major/minor axes and PA of a best-fit ellipse; (8) angular geometrical mean radius; (9) intensity-weighted mean LSR velocity; (10) intensity-weighted velocity dispersion; (11) Heliocentric distance; (12) Galactocentric distance; (13) linear geometrical mean radius; (14) surface density; (15) H_2 mass.

* These parameters were derived by an ellipse-fitting. The value in parentheses is 1σ uncertainty of each derived ellipse parameter but is replaced by the symbol ‘***’ if it is too large (larger than 180°).

† The standard deviation of the outputs from 100 iterations.

‡ The given uncertainty considers only that of the surface density (relevant to the integral of decomposed Gaussian components), not including that of distance.

§ This MC is on the edge of the HI cloud when overlaying the v -integrated CO map onto the v -integrated HI map.

–110 pc in the R_{GC} range of ~ 9 kpc to ~ 11 kpc, based on the distances provided in Tables 1 and 2. This spatial distribution is likely due to the warped Galactic plane (Burton 1988; Levine et al. 2006; Koo et al. 2017). Generally, the MCs appear to be situated within their corresponding H I superclouds, although their integrated-intensity peak positions often differ (see Section 4.1 for details).

The spatial distribution of the 26 H I clouds is illustrated in a face-on view in Figure 3. Even a cursory glance shows that the clouds are regularly distributed. The average separation between cloud (i) and its immediate neighboring clouds ($i - 1$ and $i + 1$) can be determined using the cosine law, which is given by the following equation:

$$\text{Separation} = 0.5 \sqrt{d_{i+1}^2 + d_{i-1}^2 - 2 d_{i+1} d_{i-1} \cos(\Delta l)}, \quad (7)$$

where $\Delta l = l_{i+1} - l_{i-1}$.

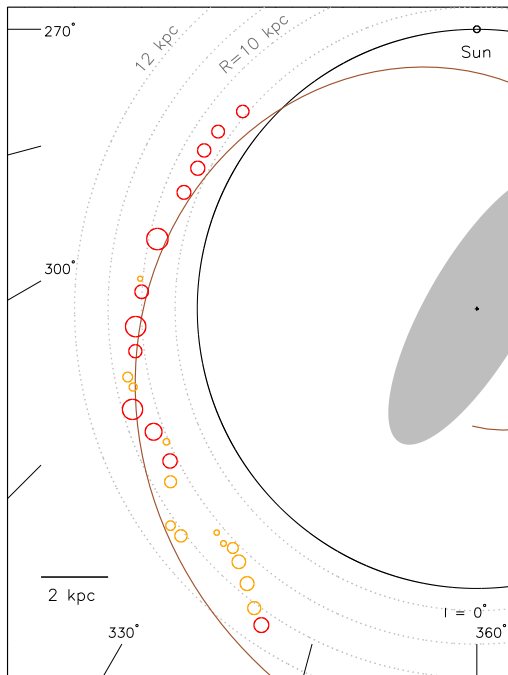


Figure 3. Schematic face-on view of the H I clouds analyzed in this paper. Circles indicate clouds of mass $\geq 5 \times 10^6 M_{\odot}$ (in red) or $< 5 \times 10^6 M_{\odot}$ (in orange). The size of each circle corresponds to the geometrical mean radius listed in Table 1. The brown curve denotes the (Sagittarius-)Carina arm spiral model, as derived by Paper I. The filled ellipse located near the Galactic center represents the central bar, as reported by (Wegg et al. 2015).

The left-hand panel of Figure 4 presents a histogram depicting this average spacing between adjacent H I clouds along the Carina arm, covering a distance of approximately 20 kpc. The bin size used for this analysis is $0.012 R_0$, which is equivalent to 100 pc, assuming $R_0 = 8.34$ kpc. The yellow histogram indicates the distribution of all H I clouds, which displays a prominent peak at $0.084 R_0$ (~ 700 pc). On the other hand, the red histogram, which represents neighboring H I superclouds with $M_{\text{HI}} \geq 5 \times 10^6 M_{\odot}$, shows a peak at $0.144 R_0$ (~ 1.2 kpc).

The separation between H I superclouds along the Carina arm has been investigated in previous studies (e.g., Efremov 1998, 2009), which corroborate our finding. It is worth noting that EE87 reported a spacing of approximately 1500 pc between H I superclouds in the first quadrant. Although this value is somewhat larger than ours, it will be still comparable, considering the use of different assumptions, such as the Sun’s location and the Galactic rotation model.

Regular segmentation in the spiral arms of nearby galaxies (Elmegreen & Elmegreen 1983) has been observed recently in M31 (Efremov 2010), M100 (Elmegreen et al. 2018), 15 other spirals (Elmegreen & Elmegreen 2019), and 3 more (Gusev et al. 2022). It has been attributed to gravitational or combined gravitational and magnetic (Parker-Jeans) instabilities in compressed spiral-arm gas (e.g., Elmegreen 1979, 1982; Kim et al. 2002; Dobbs 2008; Renaud et al. 2013; Lee & Hong 2011; Inoue & Yoshida 2019) or wobble instabilities (Wada & Koda 2004; Mandowara et al. 2022). The three-dimensional MHD simulation conducted by Lee & Hong (2011) demonstrated that when a perturbation wavelength greater than the Jeans critical wavelength acts on a self-gravitating disk of magnetized isothermal gas, the cooperation of the Parker and Jeans instabilities suppresses convection and generates a dense, large-scale structure of mass and size corresponding to the observed H I superclouds.

We introduce the concept of the ratio of *lengths* as an indicator of filament regularity and the underlying instability processes. The ratio of lengths, predicted to be around 3.9 in Elmegreen et al. (2018), represents the ratio of separation to the effective filament diameter for a non-magnetic cylinder, derived using equation 4.2 of Nagasawa (1987). While our observations do not directly measure the effective diameter or exhibit all the ideal conditions assumed in the theoretical derivation, the essence lies in capturing the regularity of the clouds and the presence of an instability mechanism rather than random cloud agglomeration. Building upon this understanding, we have considered an alternative approach to

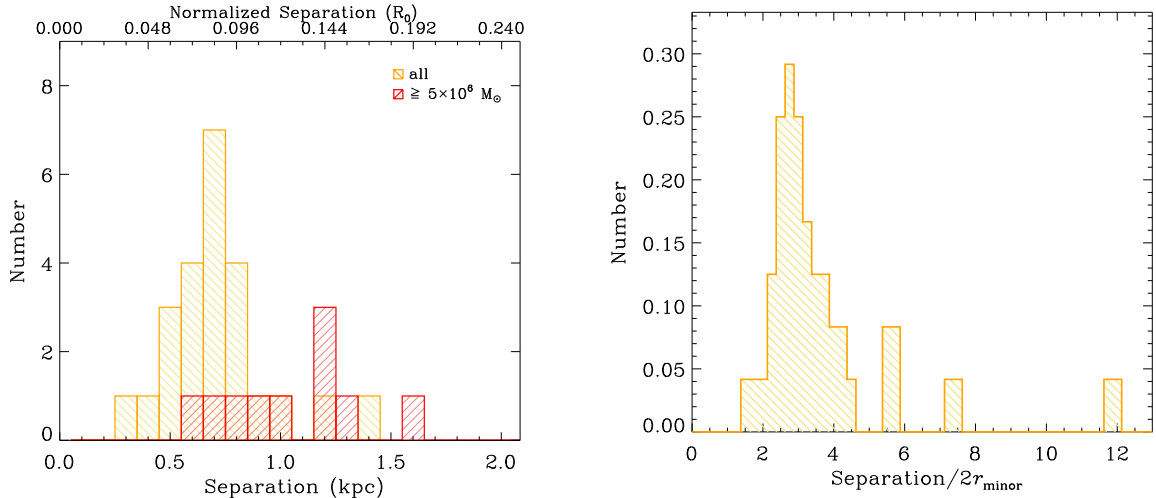


Figure 4. Histogram of the distribution of spacings between neighboring H I clouds (left), and the ratio of the separation to filament diameter (right). The filament diameter is determined as the cloud minor axis ($2r_{\text{minor}}$). The yellow sticks with left diagonals represent all twenty-six H I clouds, while the red sticks with right diagonals represent massive clouds with $M_{\text{HI}} \geq 5 \times 10^6 M_\odot$. The bin size is $0.012 R_0$, which corresponds to around 100 pc. The separation of 3.3 kpc between the last two massive clouds (H18 and H29) with $M_{\text{HI}} \geq 5 \times 10^6 M_\odot$ is not included in this plot.

assess the regularity of the clouds by focusing on the ratio of separation to the minor axis. We believe the minor axis, being a representative measure of the filament diameter, offers a closer approximation to the relevant diameter compared to the major axis. The right-hand panel of Figure 4 shows a histogram of the ratio of separation to cloud minor axis. The peak is at a ratio of around 3.

In addition, the relative separation difference (RSD), defined as the difference between two adjacent separations divided by their average, provides further insight into the regularity of cloud spacing along the filament. As described in Elmegreen et al. (2018), the relative difference in the separations between three adjacent clumps, i.e., $i - 1$, i , and $i + 1$, is

$$RSD = 2(S_{i,i-1} - S_{i,i+1}) / (S_{i,i-1} + S_{i,i+1}). \quad (8)$$

Here, S is the separation between two adjacent clouds and not the average separation between a cloud and its neighbors, as in equation 7. This RSD quantifies the deviation from equally spaced separations along the filament. This value ranges from 0 to a maximum value of 2, where a value of 0 indicates equally spaced separations and a larger value signifies a deviation from equal spacing. A peak in the histogram of these RSDs at a small value would indicate a higher level of regularity in cloud spacing, providing further evidence for the presence of instability that shapes the filamentary structures.

The RSD histogram is shown in Figure 5. The RSD peaks at ~ 0.35 . Although the observed clouds may not exhibit the same level of regularity as seen in other cases,

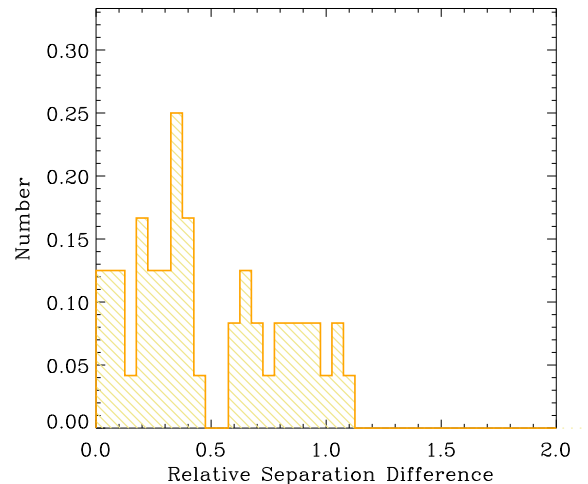


Figure 5. Histogram of the relative separation difference between clouds.

such as the well-studied M100 (Elmegreen et al. 2018), this does not diminish the significance of our findings. We can confidently state that the ratio of separation to the minor axis closely aligns with theoretical expectations, and the modest regularity observed in the RSD histogram suggests the involvement of a gravity-driven process in shaping these structures.

Figure 6 shows a theoretical distribution of separation and RSD for $N = 10^6$ points randomly placed on a line. The placement is made by assigning the point position to be a random number uniformly distributed between 0 and 1. These positions are then ordered by

increasing value and their separations determined. To account for the trend of decreasing average separation with increasing N , the separations are multiplied by N ; then the average is 1, and the separations range from 0 to some large number up to N . The separation distribution on the left of Figure 6 peaks at 0.5 with a dip toward zero separation because it is increasingly unlikely for two points to be much closer than the average separation. The RSD distribution on the right has a slowly decreasing trend toward a value of 2. This maximum occurs when all the points are at one end of the line and one point is at the other end, making $S_{i,i-1} = 0$ and $S_{i,i+1} = 1$.

Figure 5 should be compared to Figure 6 (right) because both are on relative scales. The theoretical result has 26% of the separation differences larger than 1.1 whereas the observations have none. The average RSD from theory is 0.75.

We consider the Kolmogorov–Smirnov test to determine how likely it is that the observed RSD comes from the same model as the random distribution. This test uses the normalized cumulative distributions. For the RSD, this cumulative distribution (not shown) reaches unity at the maximum difference of ~ 1.1 , from Figure 5. At this same value, the cumulative distribution for the theoretical case equals only 0.55. The difference is 0.45, which we take to be the Kolmogorov–Smirnov statistic when considering the hypothesis that the observed and theoretical distributions are from the same model. This statistic should be compared with $c(\alpha) [(N_{\text{clouds}} + N)/(N_{\text{clouds}}N)]^{0.5}$ for number of clouds in Figure 5 equal to $N_{\text{clouds}} = 26$ and $N = 10^6$ in the model. Here $c(\alpha) = [-0.5 \ln(\alpha/2)]^{0.5}$ for level $1 - \alpha$ at which the hypothesis is rejected. Setting $0.45 = c(\alpha)/(N_{\text{clouds}})^{0.5}$ for $N \gg N_{\text{clouds}}$, we derive $\alpha = 5.3 \times 10^{-5}$, meaning that the hypothesis the observed distribution is from the same model as the random distribution is rejected at a confidence level of 99.995%.

The lack of RSDs larger than 1.1 in the observations could be the result of a selection effect, where clouds that are too close to each other are called a single cloud. If we consider two nearby clouds at a separation a with another cloud a distance b from one of them, then the RSD is $2(b - a)/(b + a)$. Setting this less than 1.1 as in the observed limit gives $a > 0.29b$. If the minimum separation between two adjacent clouds is never less than 0.29 times their near-neighbor distance, we can explain the lack of high values. This type of selection effect is possible because the mean separation is ~ 700 pc from Figure 4 (left) and 0.29 times this is ~ 200 pc, which is comparable to the average major axis length of the

H I clouds, ~ 300 pc. Thus, the upper limit in Figure 5 could be because “touching” clouds have become confused with single clouds, eliminating the short spacings.

3.4. Virial Equilibrium

Determining whether H I superclouds or MCs are gravitationally bound is a fundamental question in understanding star formation. To examine the degree of self-gravitational bounding, one can compare the one-dimensional virial theorem velocity dispersion (v_{VT}) to the measured velocity dispersion (σ_v) of the H I cloud. Assuming a spherical cloud with an isothermal mass distribution, the virial dispersion is given by

$$v_{\text{VT}}^2 = \frac{GM}{4R}, \quad (9)$$

where M and R are the total mass and the radius of the complex, respectively (EE87). The factor β in Equation 18 of EE87 indicates the ratio of magnetic to turbulent pressures, and they adopted $\beta = 1$ based on the understanding that magnetism plays an important role in contributing to cloud support (see Appendix A in Elmegreen & Clemens 1985). We adopt this value, resulting in the constant in the denominator of Equation 9 being 4. M is the sum of M_{HI} in Table 1 and M_{H_2} in Table 2, and R is the geometrical mean radius of the H I cloud in Table 1. If a cloud is in virial equilibrium, the velocity ratio $v_{\text{VT}}/\sigma_v = 1$ or virial parameter (defined as $\alpha_{\text{vir}} = 4R\sigma_v^2/GM$) is equal to 1.

Figure 7 displays the velocity ratio as a function of the total cloud mass for the 26 H I clouds identified in this study. The total cloud mass ($M_{\text{HI}+\text{H}_2}$) is defined as

$$M_{\text{HI}+\text{H}_2} = M_{\text{HI}} + M_{\text{H}_2,\text{all}}, \quad (10)$$

where $M_{\text{H}_2,\text{all}}$ is the sum of masses of MCs associated with an H I cloud. The velocity ratios fall in the range of approximately 0.3–1.5, which is close to unity, indicating that some of the clouds may be gravitationally bound. For reference, if we assume a uniform density profile for the cloud in Equation 9, the constant 4 changes to 5, which results in a slightly downward of the data points shown in this figure. Comparison of CO-bright and CO-dark H I clouds reveals that CO-dark clouds generally have lower total gas mass, but the velocity ratio shows no significant difference between the two types of clouds in the mass range where both types coexist. Moreover, the velocity ratio appears to increase with increasing total gas mass, with lower-mass clouds having lower velocity ratios and higher-mass clouds having higher velocity ratios. Most of the CO-bright H I clouds have velocity ratios $\gtrsim 0.7$ ($\alpha_{\text{vir}} \lesssim 2$), suggesting that they are gravitationally bound or marginally bound. Conversely, we

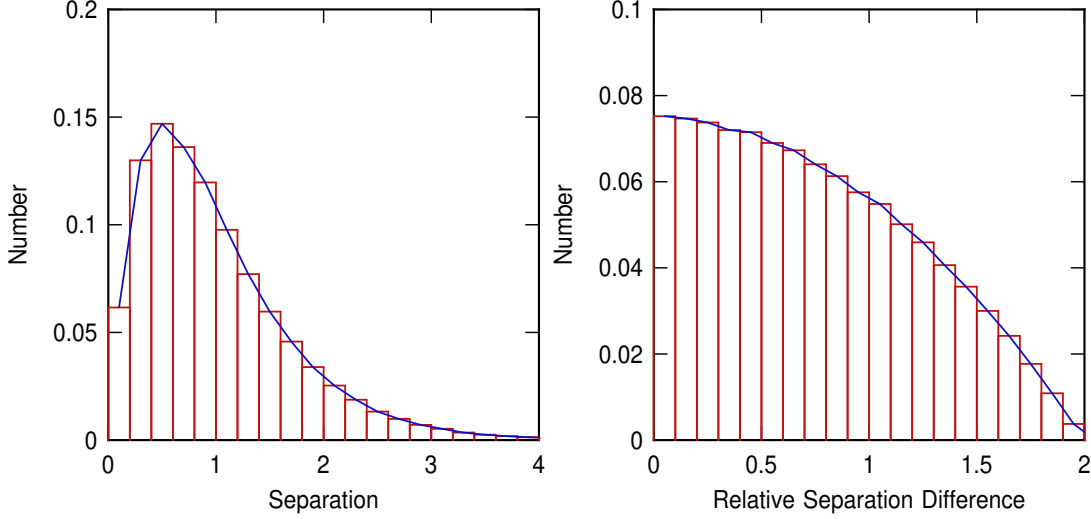


Figure 6. Theoretical model for the separation distribution (left) and the distribution of relative separation differences (right) for points uniformly distributed on a line. The units of separation in the theoretical distribution are arbitrary. The theoretical relative separation difference is non-zero above 1.1 where the observed distribution has no examples, suggesting that the observed distribution is not random. A selection effect related to cloud blending could prevent these high values.

infer that clouds with velocity ratios $\lesssim 0.5$ ($\alpha_{\text{vir}} \gtrsim 4$) are likely to be gravitationally unbound and will either expand or dissipate in the absence of confinement from external pressure.

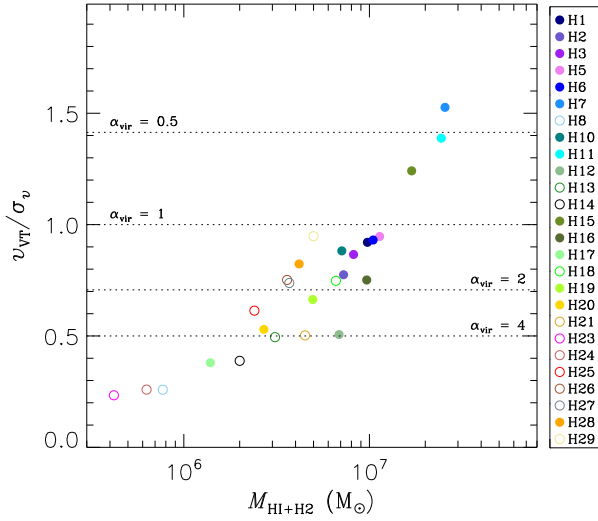


Figure 7. Relationship between the total cloud mass ($M_{\text{HI}+\text{H}_2}$) and the velocity ratio (v_{vir}/σ_v). Filled circles represent CO-bright H I clouds, while unfilled circles indicate other H I clouds. The lines mark the loci for virial parameters (α_{vir}) of 0.5, 1, 2, and 4.

In addition to examining the virial equilibrium of the H I clouds, we further investigate the relationship be-

tween the critical velocity dispersion ($\sigma_{v,\text{crit}}$) and the observed velocity dispersion (σ_v). The critical velocity dispersion is denoted as the minimum velocity dispersion required for achieving equilibrium within filamentary structure (e.g., Ostriker 1964; Inutsuka & Miyama 1992; Chandrasekhar & Fermi 1953; Stodólkiewicz 1963; Nagasawa 1987; Fiege & Pudritz 2000). It provides a measure of the velocity dispersion necessary for self-gravitational stability of the spiral arm H I to determine whether it might have collapsed into the observed clouds from a more uniform filamentary structure in the long spiral shock.

In the context of our study, we consider the critical velocity dispersion as a key parameter for assessing the gravitational stability of the H I in the spiral arm before it formed the observed superclouds. The critical velocity dispersion is determined based on the equilibrium mass (μ) per unit length.

$$\sigma_{v,\text{crit}}^2 = G\mu/2. \quad (11)$$

We estimate μ as the total gas mass ($M_{\text{HI}+\text{H}_2}$) divided by the spacing between the clouds which is derived using Equation 7. This approach allows us to identify the minimum velocity dispersion required to maintain a state of equilibrium within the Carina arm.

Figure 8 presents a scatter plot of $\sigma_{v,\text{crit}}$ versus the σ_v for the H I clouds analyzed in this work. The corresponding histograms illustrate the distributions of the critical and observed velocity dispersions. Notably, the observed velocity dispersions, calculated from bright-

ness temperature-weighted measurements, exhibit a relatively constant behavior. The critical dispersion averages around 4 km s^{-1} . If the observed clouds formed by gravitational instabilities in a previously more uniform spiral arm gas, then the velocity dispersion in this gas had to be less than or equal to $\sim 4 \text{ km s}^{-1}$ for this process to be rapid. Such a decrease is expected theoretically (Cowie 1981; Dobbs et al. 2008) and there are indications of a low dispersion for the cool component H I in observations of spiral galaxies by Ianjamasimanana et al. (2012). The higher observed velocity dispersions in present-day H I clouds suggest the presence of additional energy sources, such as gravitational energy from their formation or young stellar feedback after stars appeared.

4. H I SUPERCLOUDS AND MOLECULAR CLOUDS

4.1. *Spatial Relation between H I Superclouds and MCs*

The formation of molecular clouds from H I gas is a complex process that can be driven by a combination of physical processes, such as turbulent compression and fragmentation (which create density fluctuations), radiative compression (which triggers thermal instability), gravitational instability (which enhances self-gravity), and magnetic instability (which can contribute to cloud collapse and fragmentation) (e.g., Kwan & Valdes 1987; Elmegreen 1996; Hennebelle & Péroul 2000; Ostriker & Kim 2004; Dobbs et al. 2014). While the classical understanding of the spatial distribution of H I and molecular gas is a layered structure with a giant molecular cloud surrounded by atomic gas (Blitz 1993), the resulting spatial distribution of molecular clouds relative to their parent H I clouds is expected to depend on a variety of factors, including the specific physical conditions of the gas and the relative importance of these formation mechanisms. However, the ubiquity of H I gas in the Galactic disk and the difficulty in determining its exact kinematic distance along the line of sight makes it challenging to establish a definitive association between H I and molecular clouds and to provide observational insight. Nevertheless, it is worthwhile to investigate the spatial distribution of H I superclouds and MCs, particularly in the outer Carina arm, which is relatively well-identified.

A simple question arises as to whether the detected MCs are centered on the associated H I superclouds or matched with local H I emission peaks. Extragalactic observational studies of the spatial distribution and kinematics of molecular clouds relative to their associated H I gas have been conducted using a variety of tracers, such as CO and H I emission (e.g., Wong et al. 2009;

Tosaki et al. 2011). It is found that CO emission was typically associated with high-intensity H I gas, but not all regions of high H I intensity were found to have CO emission.

Figure 9 displays a position-velocity diagram of H I and CO emission features, which is averaged over latitudes. The H I cloud emission features defined in this work are generally visible within the gray contour of 30 K (see Section 3.1.1 and Figure 1 for details). The CO emission features, displayed with bright gray contours, are commonly placed in the velocity range where the H I cloud features are visible, although some small and weak CO emission features at $l \gtrsim 320^\circ$ do not appear in this averaged diagram. Extended, an arc-like feature in H I emission is observed at $l \sim 296^\circ$ to 300° and $v_{\text{LSR}} \sim 35$ to 60 km s^{-1} , which appear as a ring-like structure when lower velocity H I gas is included. However, this feature is not within the scope of this study. This may indicate activity such as a supershell or chimney, and is very likely to be related to GSH 298–01+35, proposed as a chimney structure, identified by McClure-Griffiths et al. (2002). A detailed 3D kinematic analysis would provide further insight into the structures of the H I and molecular gas.

Figure 10 presents a comparison of the H I and CO emission features in a position-position diagram. The figure shows the ratio of column densities between H_2 column density (N_{H_2}) and H I column density (N_{HI}) obtained by using Figure 2(a). The column density ratio, $2N_{\text{H}_2}/N_{\text{HI}}$, is beneficial for studies of molecular clouds and star formation, as it reflects the degree of molecular gas enrichment in a given region, which refers to the proportion of molecular gas present relative to atomic gas. This parameter is important for understanding the conditions necessary for star formation. The color image displays the column density ratio with contours indicating N_{HI} from 2.2 to $4.8 \times 10^{21} \text{ cm}^{-2}$ for the top panel, and N_{H_2} from 5 to $60 \times 10^{20} \text{ cm}^{-2}$ for the bottom panel. The column density ratios were calculated only where N_{H_2} is greater than or equal to $5 \times 10^{20} \text{ cm}^{-2}$, which is equal to the minimum limit for the identification of MCs in the work. The v -integrated positions of all CO emissions of the identified MCs are equal to where column density ratios are expressed. The column density ratios displayed in this figure range from approximately 0.2 to 3.2, with the highest value observed at M31 in association with H7.

The minimum value for H I column density used to identify H I clouds in this study may provide insight into areas where H_2 formation occurs more efficiently through self-shielding. Numerous previous studies have demonstrated that the saturation of H I column density

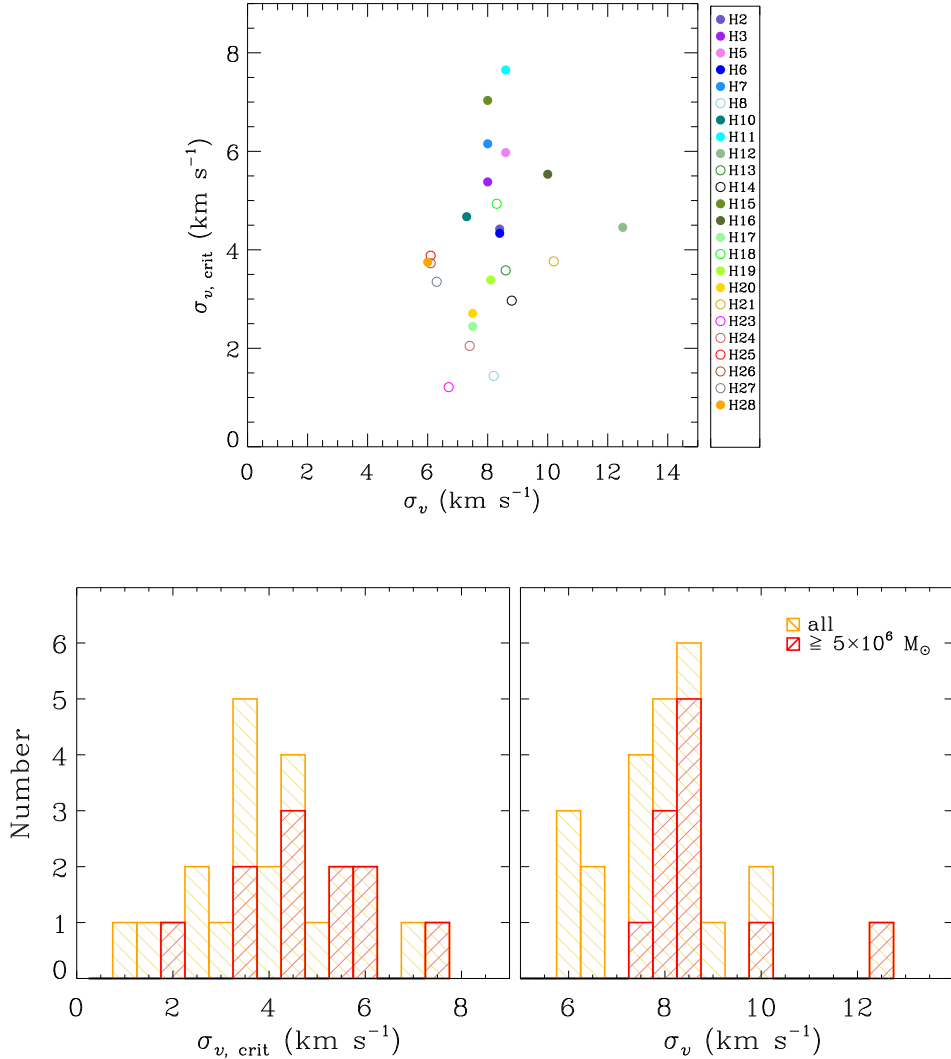


Figure 8. Scatter plot of critical velocity dispersion ($\sigma_{v, \text{crit}}$) and observed velocity dispersion (σ_v), with histograms of each. The left histogram displays the distribution of $\sigma_{v, \text{crit}}$, while the right histogram shows the distribution of σ_v . In the histograms, the yellow sticks with left diagonals represent all H I clouds, whereas the red sticks with right diagonals represent massive clouds with $M_{\text{HI}} \geq 5 \times 10^6 M_{\odot}$. The bin size for both histograms is set to 0.5 km s^{-1} .

at $\approx 10^{21} \text{ cm}^{-2}$ in the correlation between H I column density and tracers of total gas column density, such as infrared surface brightness and optical reddening, indicates the presence of H_2 (e.g., Reach et al. 1994; Meyerdierks & Heithausen 1996; Barriault et al. 2010; Liszt 2014; Park et al. 2018). However, it is important to note that the conversion from atomic to molecular gas can also be influenced by other factors, such as metallicity (Bolatto et al. 2013, and references therein).

Most of the MCs appear to be spatially associated within the corresponding H I superclouds, but a majority of them are not situated in the central regions of these superclouds. Notably, many peaks in CO emission appear somewhat distant from the nearby H I emission

peaks. It should be noted that some MCs (e.g., H47 at $l \simeq 326^\circ$ and H48 at $l \simeq 328^\circ$) are found to be situated at or beyond the periphery of the relevant H I supercloud. Although the cloud boundary, particularly for H I superclouds, was arbitrarily delineated based on bright, dense regions, the physical associations of the aforementioned cases may be less clear than those of other cases. Nonetheless, we have included those MCs in the catalog.

As seen in the bottom panel in Figure 10, N_{H_2} is positively correlated with the column density ratio. That is, the CO emissions peak in regions with high column density ratios, indicating that the conversion of H I to H_2 is more efficient in those regions. This may be due

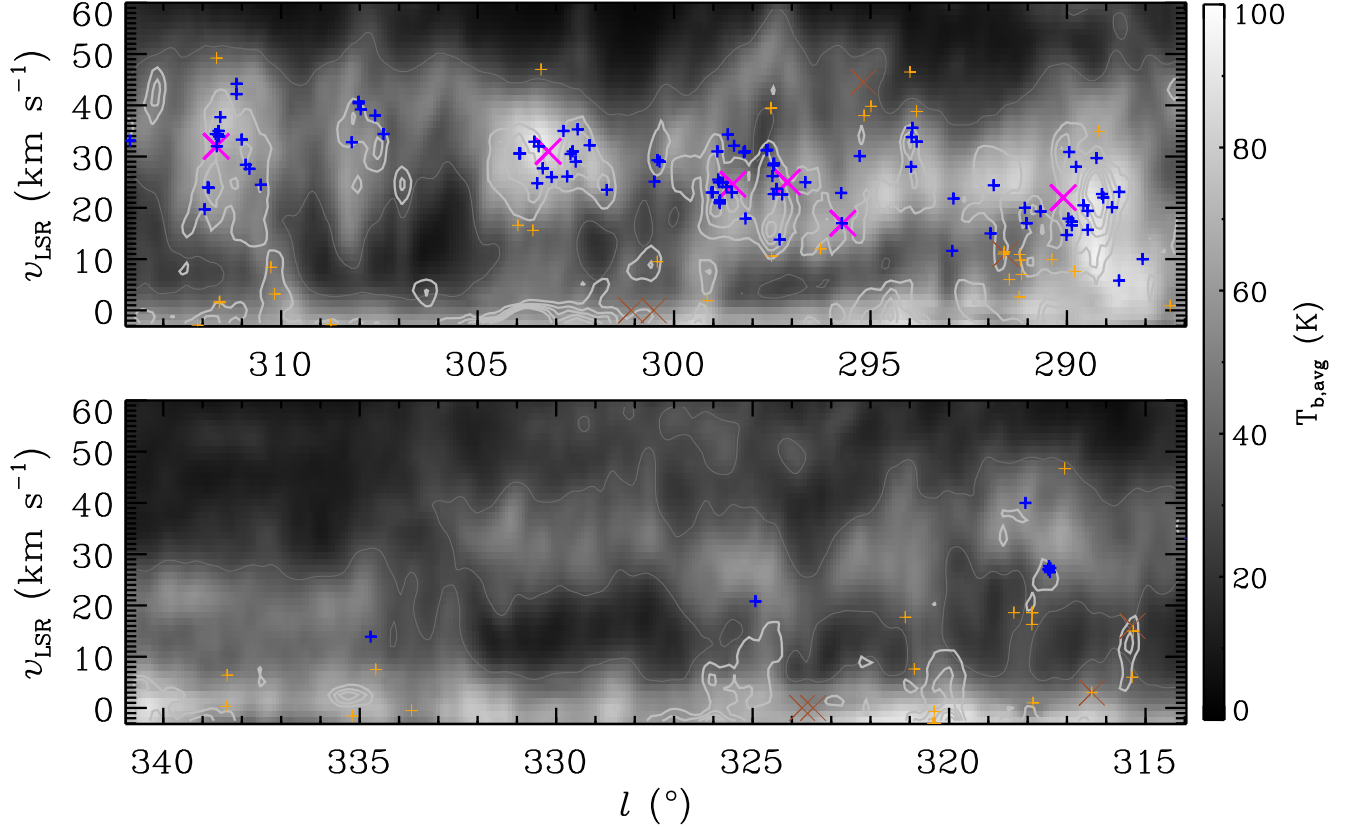


Figure 9. b -averaged (l, v_{LSR}) H I map, overlaid with CO contours and star-forming regions. The integrated latitude range for the map is from -2° to $+1^\circ$. The background image with a thin, dark gray contour represents H I, and the contour level is set at 30 K. CO contours, displayed as thick, bright gray lines, indicate levels of 0.1, 0.2, 0.3, 0.4, and 0.5 K. *WMAP* sources, likely related to the outer Carina arm, are marked with thick, blue pluses, whereas thin, orange pluses represent those that are unlikely to be related. Similarly, thick, magenta crosses represent *WISE* H II regions with a single measured velocity, likely associated with the outer Carina arm, while thin, brown crosses indicate those that are unlikely to be related.

to certain physical conditions that favor the formation of molecular gas, such as high gas density or low gas temperature. However, as seen in the top panel in Figure 10, the correlation between column density ratios and local H I peaks seems lacking. This may be due to various factors. One possible explanation is that the conversion of H I to H₂ is not solely determined by the local H I column density but also by other physical conditions such as gas density, temperature, radiation field, and turbulence or magnetic fields. In regions where the physical conditions are favorable for forming molecular gas, the conversion may be more efficient even if the local N_{HI} is not high. On the other hand, in regions where the physical conditions are unfavorable, the conversion may be less efficient even if the local N_{HI} is high. It is possible that triggered molecular cloud formation could play a role in the lack of correlation between the column density ratios and local H I peaks. When molec-

ular clouds form due to external triggering mechanisms, such as shock compression or radiation from massive stars, the conversion from H I to H₂ can happen more efficiently in certain regions that are influenced by these triggering mechanisms (e.g., Ballesteros-Paredes et al. 1999; Hartmann et al. 2001; Inoue & Inutsuka 2009; Inutsuka et al. 2015). This can lead to molecular gas being present in regions with lower H I column densities or in regions where the H I gas has been dispersed or compressed by the triggering event.

Figure 11 presents a quantitative comparison between the positions of H I clouds and MCs. The left group of three panels shows the projected distances on the sky in angular scale, with an adopted angular bin size of $8'$, which is approximately half of the angular resolution of the data used. The right group of three panels displays the distances computed using the heliocentric distance of the corresponding H I cloud provided in Ta-

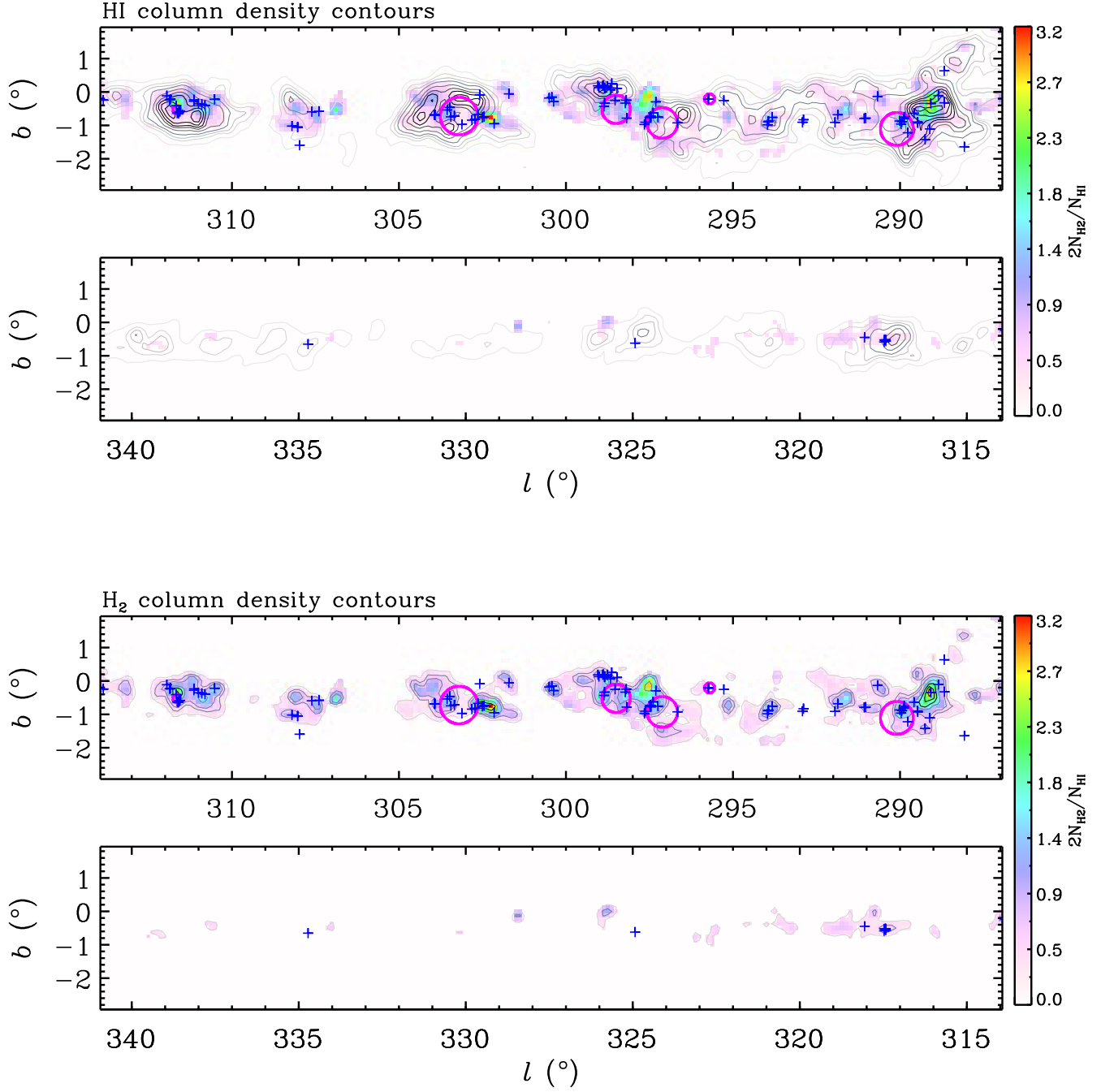


Figure 10. Ratio map of H₂ column density (N_{H_2}) to H I column density (N_{HI}), specifically $2N_{\text{H}_2}/N_{\text{HI}}$, overlaid with the H I column density contours (top) or H₂ column density contours (bottom). The white areas in both the top and bottom panels indicate regions where $N_{\text{H}_2} < 5 \times 10^{20} \text{ cm}^{-2}$, which corresponds to the minimum threshold for MC identification, and have been masked. We also masked the area of $l > 291^\circ$ and $b < -2^\circ$ or $b > 0.8^\circ$. Some weak CO emission features are visible in the region, but their validity is uncertain as they were obtained by different surveys with relatively low sensitivity and a large sampling value. The contours are color-graded from gray to black to indicate increasing levels. In the top panel, the N_{HI} levels are 2.2, 2.7, 3.0, 3.3, 3.7, 4.0, 4.2, 4.4, 4.6, $4.8 \times 10^{21} \text{ cm}^{-2}$. In the bottom panel, the N_{H_2} levels are 5, 10, 15, 30, 40, 50, $60 \times 10^{20} \text{ cm}^{-2}$. The star-forming regions, which are likely related to the outer Carina arm, are represented by magenta circles and blue pluses for *WMAP* sources and *WISE* H II regions, respectively, as shown in Figure 9. The size of each circle for the *WMAP* sources corresponds to their respective effective radii.

ble 1, presented in linear scale with an arbitrarily selected linear bin size of 25 pc. According to the cloud definition method in this paper, the emission peaks of MCs (MC_P) are typically located at or near the centers of the MCs (MC_C), given the angular resolution (panel (b)). In contrast, the local emission peaks of H I clouds (HC_{LP}) are not always situated at their centers (HC_C) (panel (a)), and some clouds even exhibit multiple peaks (e.g., H7 and H11). When comparing MC_P with HC_C , we observe that most MC_P are significantly distant from HC_C (green in panel (c)). Additionally, we identified the nearest H I peak for a given MC and labeled it as $HC_{NP,MC}$, then measured the distance between them (yellow in panel (c)). The distribution of MC_P – $HC_{NP,MC}$ exhibits a relatively stronger correlation than that of the MC_P – HC_C and displays two prominent peaks with a valley around the mean mutual distances of $\sim 23'$. Specifically, 17 pairs on the left side of the distribution exhibit a strong positional correspondence or marginal overlap, while the remaining 31 pairs show a clear positional discrepancy.

4.2. Molecular Mass Fraction of H I Superclouds

In Figure 12, we present two distributions showing the molecular mass fraction as a function of Galactocentric distance (left panel) or total gas surface density (right panel) of H I superclouds. The molecular mass fraction, f_{H_2} , is defined as

$$f_{H_2} = \frac{M_{H_2,all}}{M_{HI} + M_{H_2,all}}. \quad (12)$$

The total gas surface density, Σ_{HI+H_2} , is defined as

$$\Sigma_{HI+H_2} = \frac{M_{HI} + M_{H_2,all}}{A_{HI}}, \quad (13)$$

where A_{HI} is the area of a H I supercloud (see Section 3.2.1).

As anticipated, a larger mass of an H I cloud is generally associated with a larger mass of an MC. The relation between f_{H_2} and Σ_{HI+H_2} exhibits a clear positive correlation. In regions where the Σ_{HI+H_2} is higher, there is generally a higher pressure environment, which facilitates the conversion of atomic gas into molecular gas. The positive correlation between f_{H_2} and Σ_{HI+H_2} can be understood within the context of interconnection processes that drive the conversion of atomic hydrogen into molecular hydrogen and ultimately lead to star formation.

Furthermore, previous studies, such as Elmegreen & Elmegreen (1987), have observed a trend where the value of f_{H_2} decreases as the Galactocentric distance increases. In our study, we observe this trend in the

outer Carina arm clouds spanning $l = 288^\circ$ to 340° , which extends over the Galactocentric distance range of $R_{GC} \sim 9$ –11 kpc. We find that the decrease in f_{H_2} smoothly declines with increasing R_{GC} , with few deviations. Additionally, the majority of H I superclouds with $f_{H_2} > 0.1$ or $\Sigma_{HI+H_2} \gtrsim 60 M_\odot pc^{-2}$ exhibit evidence of star-forming activity, as indicated by the presence of H II region(s). The f_{H_2} values of H I superclouds between $R_{GC} \sim 9$ –10 kpc exhibit a relatively wide distribution ranging from ~ 0.1 to 0.3, suggesting that variations in f_{H_2} may be influenced by local environmental factors or other processes affecting the conversion of atomic to molecular gas. For example, higher gas densities in some H I superclouds might lead to increased molecular mass fractions and consequently promote star formation. In contrast, the range of 0.1–0.3 at $R_{GC} \sim 9$ –10 kpc is somewhat larger than the f_{H_2} values (< 0.1) of solar-neighborhood H I superclouds reported by Elmegreen & Elmegreen (1987). It is worth noting, however, that the mean f_{H_2} value over the entire gas disk, integrated over b from -30° to $+30^\circ$, at the solar radius is 0.1–0.2, while it increases to ~ 0.5 at the Galactic midplane when integrated over $b = -1.5^\circ$ to $+1.5^\circ$ (Koda et al. 2016). This observation underscores the importance of considering the relationship between molecular mass fraction, gas surface density, and the presence of H II regions in understanding star formation processes within these superclouds.

5. STAR FORMATION

5.1. Spatial Relation of H II regions with H I Superclouds and MCs

The presence of H II regions is a strong indicator of the existence of high-mass star-forming regions. To investigate the relationship between H I superclouds and H II regions in the outer Carina arm, we overlaid the H II regions, obtained from the H I catalog, in the outer Galaxy onto b -averaged (l, v) or v -integrated (l, b) diagrams of Figures 9 and 10. We used star-forming regions including those cataloged by Lee et al. (2012a) using Wilkinson Microwave Anisotropy Probe (*WMAP*) data and the H II regions identified in the outer Galaxy from the all-sky Wide-field Infrared Survey Explorer (*WISE*) survey (Anderson et al. 2014)⁴. Specifically, we focused on H II regions with a single observed velocity. In Figure 9, the associations of two objects, namely *WISE* H II regions and *WMAP* sources, with the outer Carina arm are indicated through different symbols and line thicknesses. The associations are determined based on

⁴ We used Version 2.0

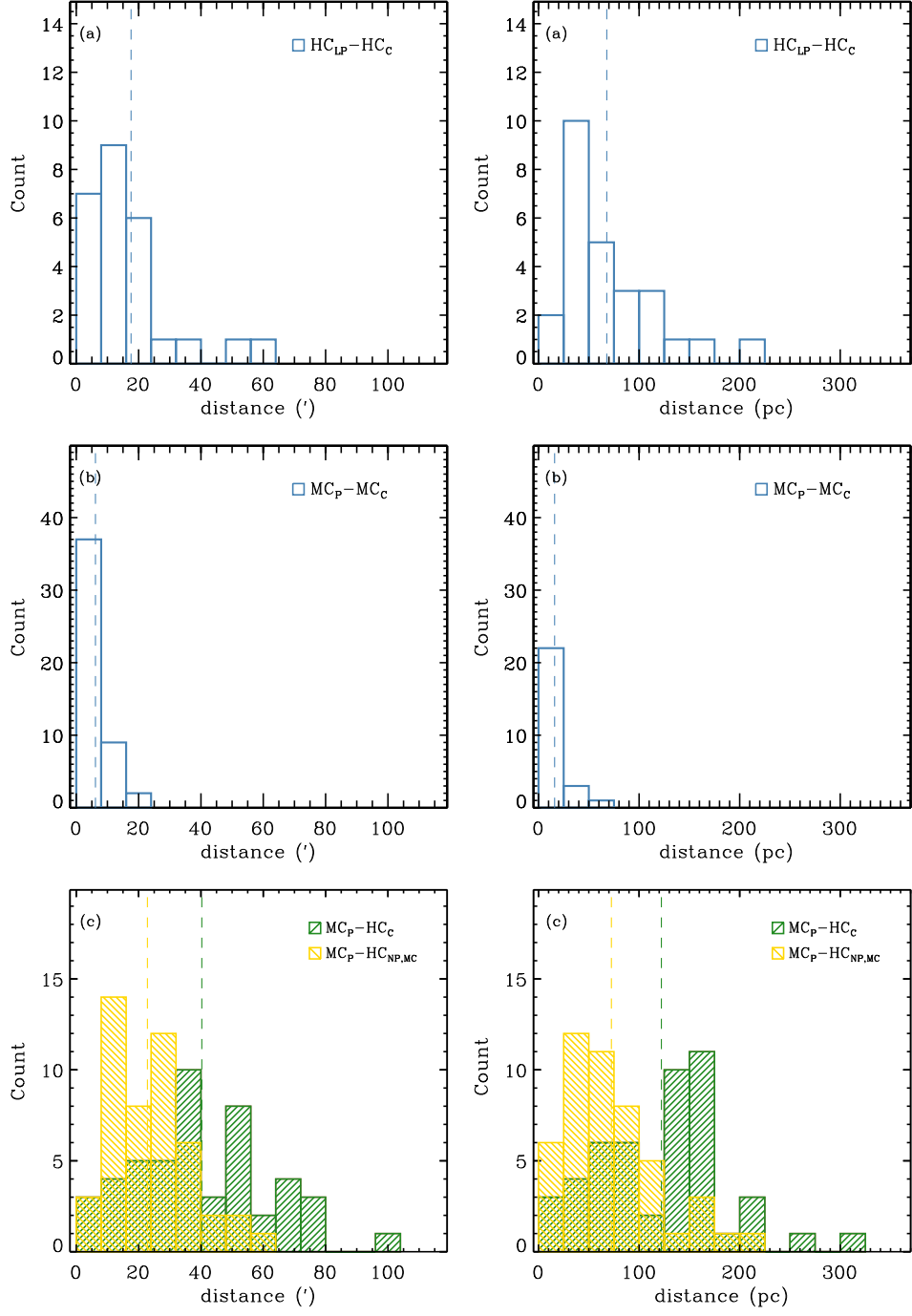


Figure 11. Histogram of the mutual distances between different positions, including: (a) the local emission peaks of H I clouds (HC_{LP}) and the geometric centers of the H I clouds (HC_C) ($HC_{LP}-HC_C$), (b) the emission peaks of MCs (MC_P) and the geometric centers of the MCs (MC_C) (MC_P-MC_C), and (c) the emission peaks of MCs (MC_P) and either the geometric centers of MC-related H I clouds (HC_C) (MC_P-HC_C ; green with right diagonals) or the local emission peaks of H I clouds nearest the MCs ($HC_{NP,MC}$) ($MC_P-HC_{NP,MC}$; yellow with left diagonals). The left group of four panels shows the distances projected in the sky in angular scale, and the right group shows the distances calculated assuming the heliocentric distance of relevant H I cloud, provided in Table 1, in linear scale. These result in the minimum values, which are not the actual separation in 3D. The emission peaks were derived from v_{LSR} -integrated maps (e.g., Figure 2(a)). For the left panels, we chose a bin size is $8'$, which is approximately half of the angular resolution of the data used. The right panels, on the other hand, were binned with an arbitrary bin size of 25 pc. A vertical dotted line marks the mean value of each case (the parentheses refer to the right panel): (a) $18'$ (68 pc), (b) $6'$ (16 pc), (c) $23'$ (72 pc); $40'$ (122 pc). The two mean values for the left and right panels do not correspond directly to each other since the distances to the H I clouds are different.

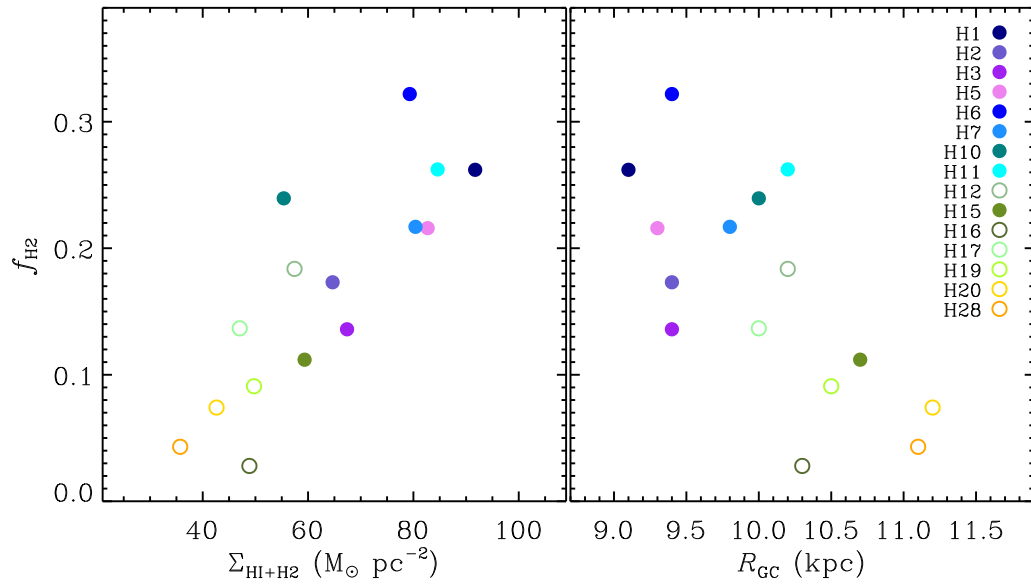


Figure 12. Relation of the molecular mass fractions (f_{H_2}) and the total gas surface densities ($\Sigma_{\text{HI}+\text{H}_2}$) of H I superclouds (left) or their Galactocentric distances (right). Filled symbols indicate H I superclouds associated with H II region(s), while unfilled symbols represent H I superclouds without H II region(s).

a simple comparison of observed LSR velocities. *WISE* H II regions are represented by pluses, marked in blue or orange, with varying line thickness. The thicker blue pluses correspond to likely associations with the outer Carina arm, while the thinner orange pluses indicate likely no association. Similarly, *WMAP* sources are depicted as crosses in magenta or brown, with different line thicknesses. The magenta crosses with thicker lines indicate likely associations, while the thinner brown crosses do not exhibit a clear association. Figure 10 specifically highlights the blue pluses for *WISE* H II regions and marks *WMAP* sources likely related to the outer Carina arm with magenta circles. The circle size of each *WMAP* source represents its effective radius. Most of the H II regions appear to be associated with the outer Carina arm, suggesting a clear positional correlation between the three components: H I superclouds, GMCs, H II regions.

Upon closer examination, we found that eleven H I superclouds (H1–3, H5–7, H10–11, H15, H18, and H25) are associated with *WISE* H II regions, indicating ongoing high-mass star formation. However, we were unable to detect any CO emission, which is commonly used as a tracer of molecular gas, associated with two of them (H18 and H25). This could imply that either the molecular gas in these regions is not abundant enough to be traced by CO emission or that the CO emission is too weak to be detected with our current observations.

The spatial distribution of star-forming regions relative to their associated H I supercloud is also not centralized. However, these regions are typically located within the range of the H I supercloud and distributed closer to the CO emission peaks. This is a natural phenomenon as stars form in dense regions of MCs. Murray & Rahman (2010) proposed that the *WMAP* sources are bubbles generated by massive star clusters, representing the extended low-density H II regions previously described by Mezger (1978). Furthermore, they found that classical giant H II regions are distributed in the bubble walls, which can be explained by triggered star formation. H7 provides a good example of such a scenario, where a *WMAP* source is located in the center of H7, which exhibits low N_{HI} and N_{H_2} . Several *WISE* H II regions are located near the effective radius boundary of the *WMAP* source and are closer to the CO emission peaks. Based on these facts, we propose that the earlier star formation at the cloud center produced the *WMAP* bubble, which then triggered the next star formation event in the *WISE* H II regions. Additionally, it is likely that the atomic and molecular gases in the cloud center were blown away during this process.

The results of the comparison between the centers of *WISE* H II regions and MC_{P} , HC_{C} , or $\text{HC}_{\text{NP,MC}}$ are shown in Figure 13. The mean mutual distances increase from MC_{P} to $\text{HC}_{\text{NP,MC}}$, and their distributions exhibit some differences (red, yellow, and green, respectively). We found that the degree of correlation with the central positions of the H II regions follows the order of $\text{HC}_{\text{NP,MC}} < \text{HC}_{\text{C}} < \text{MC}_{\text{P}}$. Notably, the distribution of H II region– MC_{P} is positively skewed by numerous pairs with lower values than their mean, suggesting a strong positional correspondence or marginal overlap for many pairs. These results indicate that H II regions are more closely related to emission peaks of MCs than those of H I clouds. This is consistent with the fact that stars form within the densest cores within MCs, and the ionizing radiation from young massive stars creates H II regions within or near the MCs. On the other hand, as stars form and evolve, stellar feedback, such as radiation pressure, stellar winds, and supernova explosions, can remove the surrounding gas and dust, potentially influencing the correlation between the central positions of H II regions and emission peaks of MCs. However, our angular resolution might not be high enough to resolve the detailed effects of stellar feedback, especially for targets at distances over 7 kpc. Also, there is a limitation in the examination of correlation in 2D space integrated along velocity. Despite these limitations, our findings are in line with the general understanding that H II regions are more closely related to MCs than large, diffuse H II clouds. The fact that 67 out of 106 pairs ($\sim 63\%$) in the H II region– MC_{P} distribution show good matching supports the notion that H II regions and MCs are physically associated with each other.

5.2. Star Formation Rate

The star formation rate (SFR) in the Galactic star-forming regions has been extensively studied in the literature, often using free-free emission flux measured from *WMAP* (Murray & Rahman 2010; Lee et al. 2012a). In this work, we use physical information of star-forming complexes (SFCs) cataloged by Lee et al. (2012a). We match seven SFCs to six H I superclouds, and their catalog numbers are listed in Table 3. We derive SFRs from the total ionizing photon luminosity (Q) using the following equations, which are similar to Equations (3), (9)–(10) of Lee et al.:

$$\frac{\text{SFR}}{(\text{M}_{\odot} \text{ yr}^{-1})} = 4.1 \times 10^{-54} Q, \quad (14)$$

$$\frac{Q}{(s^{-1})} = 1.34 \times 10^{26} \times \left(\frac{4\pi d^2 F_{\nu}}{\text{erg s}^{-1}} \right) \times 1.37, \quad (15)$$

where 1.37 is a correction factor accounting for the absorption of ionizing photons by dust grains, and the term

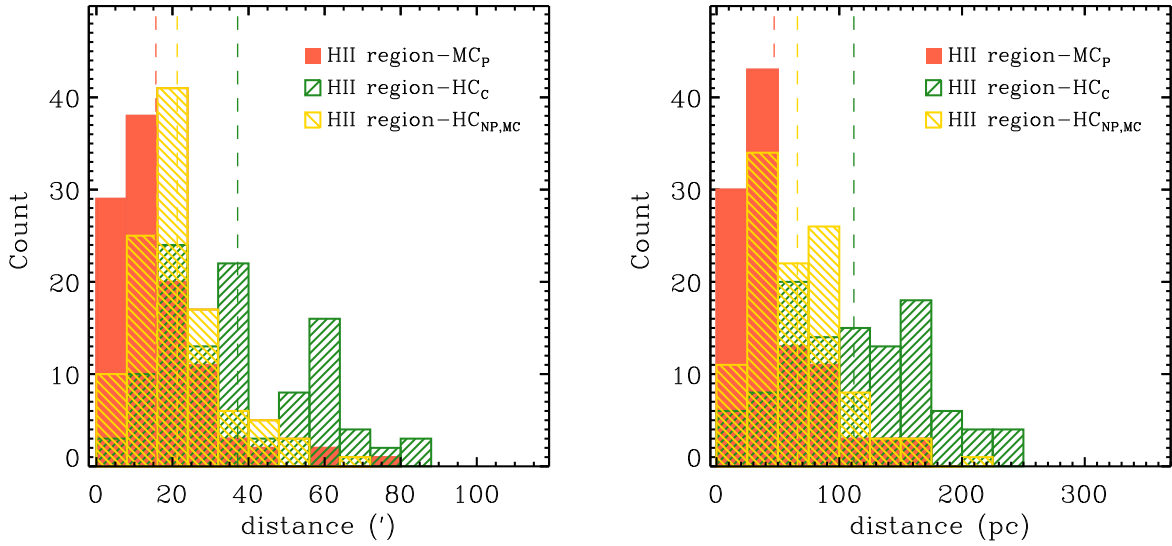


Figure 13. Histogram similar to Figure 11, but for the mutual distances between different positions, the centers of *WISE* H II regions and either MC_P (H II region- MC_P ; red filled) or HC_C (H II region- HC_C ; green with right diagonals) or $HC_{NP,MC}$ (H II region- $HC_{NP,MC}$; yellow with left diagonals). Vertical dotted lines mark mean values of 16' (47 pc); 21' (66 pc); 37' (112 pc), with the values in parentheses corresponding to those for the right panel.

of $4\pi d^2 F_\nu$ describes the specific free-free luminosity at 94 GHz of a given H II region, which is calculated with the 94 GHz free-free flux cataloged in Table 1 of Lee et al. and its recalculated distance. The distances were derived using the velocities given in Lee et al. and the flat Galactic rotation model adopted in this work. Table 3 lists Q , SFR, and surface densities of SFR, molecular gas, and total gas (Σ_{SFR} , Σ_{H_2} , and Σ_{HI+H_2}) derived for a given H I supercloud. The surface densities are based on the area of a matched H I supercloud, e.g., $SFR \times A_{HI}^{-1}$ as similar to Equation 13.

The empirical relationship well-known as the Kennicutt-Schmidt (K-S) law (Schmidt 1959; Kennicutt 1989, 1998) describes a power-law relation between gas surface density and SFR surface density. The original K-S relation uses the total gas surface density, which includes both atomic and molecular gas. It appears still prominent in the global galaxy scale, that is, disk-averaged (Kennicutt & Evans 2012, reference therein). However, in some cases, variations of the K-S relation focus on molecular gas only, as molecular gas is more directly related to star formation. For example, Bigiel et al. (2008) studied the relationship between Σ_{SFR} and Σ_{HI} or Σ_{H_2} at sub-kpc scales within nearby spiral galaxies. They found that Σ_{SFR} correlates well with Σ_{H_2} , but shows little or no correlation with Σ_{HI} . Similar results known as the resolved K-S relation have

been reported by other extragalactic studies (e.g., Leroy et al. 2008; Schruba et al. 2011; Williams et al. 2018).

Figure 14 presents the relation between the SFR surface density (Σ_{SFR}) and the surface densities of H I (Σ_{HI}), H II (Σ_{H_2}), or total gas (Σ_{HI+H_2}) in H I superclouds (referred to as $\Sigma_{SFR}-\Sigma_{HI}$, $\Sigma_{SFR}-\Sigma_{H_2}$, and $\Sigma_{SFR}-\Sigma_{HI+H_2}$, respectively). As shown in the previous studies, we also find that Σ_{SFR} appears independent of Σ_{HI} and Σ_{HI+H_2} in H I superclouds. The correlations are weak, with ρ of -0.029 and p-value of 0.96 for both. Although our findings are limited to a very small number of samples, they are still meaningful to compare to others. Since the H I component dominates the total gas content for our H I superclouds, the $\Sigma_{SFR}-\Sigma_{HI+H_2}$ relation follows the $\Sigma_{SFR}-\Sigma_{HI}$ trend closely. Our finding of no-correlation in $\Sigma_{SFR}-\Sigma_{HI}$ and $\Sigma_{SFR}-\Sigma_{HI+H_2}$ is consistent with those obtained by Lada et al. (2013) for local GMCs in the Milky Way. They explained their findings as a characteristic of constant gas surface density for Galactic GMCs (e.g., Lombardi et al. 2010; Heyer et al. 2009), which might also be acceptable to our result of H I superclouds.

On the other hand, we do observe a positive correlation between Σ_{SFR} and Σ_{H_2} , similar to the resolved K-S relation, although this correlation can be less clear due to a small number of data points. Spearman's rank correlation coefficient of 0.54 and p-value of 0.27 also indicate a moderate positive correlation. The power-law index of ~ 1.3 we found is in good agreement with

Table 3. Star Formation Properties of H I Superclouds

	Q	SFR	Σ_{SFR}^a	$\Sigma_{\text{H}_2}^a$	$\Sigma_{\text{HI+H}_2}^a$	Lee SFC ^b
# _{HI}	(s ⁻¹)	(M _⊙ yr ⁻¹)	(M _⊙ pc ⁻² Myr ⁻¹)	(M _⊙ pc ⁻²)	(M _⊙ pc ⁻²)	
H1	1.3e+51	5.4e-03	1.050	24.0	91.7	167
H3	4.6e+50	1.9e-03	0.016	9.2	67.4	171
H5	2.4e+51	9.9e-03	0.071	17.9	82.7	172, 173
H6	4.3e+51	1.8e-02	0.134	25.5	79.3	174
H7	4.4e+51	1.8e-02	0.057	17.4	80.4	181
H11	1.2e+51	4.9e-03	0.017	22.2	84.6	192

^a All surface densities are based on the area of a matched H I supercloud.

^b SFC(s) cataloged in Lee et al. (2012a) which is/are matched to a given H I supercloud.

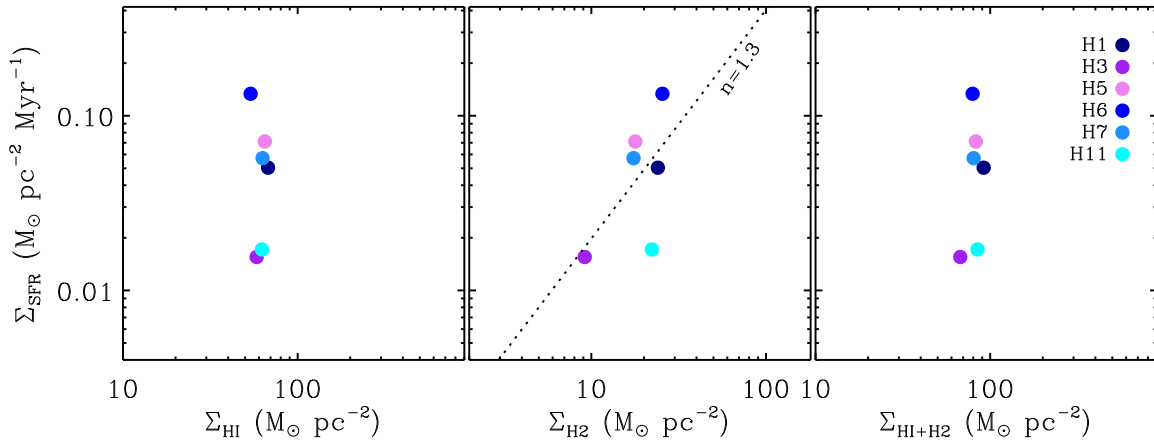


Figure 14. Relation between the SFR surface density (Σ_{SFR}) and the surface densities of H I (Σ_{HI} ; left), H₂ (Σ_{H_2} ; middle), or total gas ($\Sigma_{\text{HI+H}_2}$; right) in six H I superclouds. All surface densities in this plot were calculated based on the area of a matched H I supercloud. In the middle panel, the best single power-law fit with a power-law index of $n \simeq 1.3$ is marked with a dotted line.

the well-known value of ~ 1.4 for the global K-S relation Kennicutt (1998). This consistency implies that the star formation process in our study region follows a similar scaling relation as observed on global scales in other galaxies. Our results are also consistent with the findings of Bigiel et al. (2008) and Leroy et al. (2013), who demonstrated that molecular gas plays a dominant role in regulating star formation across a wide range of spatial scales and environments. This reinforces the importance of molecular gas in regulating star formation and provides additional support for the K-S relation as a fundamental scaling law governing the conversions of gas into stars.

6. SUMMARY

In this study, we investigated H I clouds, MCs, and star formation in the Carina spiral arm of the outer Galaxy.

Using HI4PI survey and CfA CO survey data, we identified H I clouds and MCs based on (l, v_{LSR}) locations of the Carina arm obtained from Paper I. We derived physical parameters, including size, mass, and distance, for 29 H I clouds and 49 MCs, but conducted further analysis on 26 H I clouds and 48 MCs (see Section 3.1.1).

Most of the identified H I clouds are more massive than $10^6 M_{\odot}$ and are referred to as H I superclouds. Fifteen of the 26 H I clouds have associated MC(s) with masses exceeding $10^6 M_{\odot}$ with $\Sigma_{\text{HI+H}_2} \gtrsim 50 M_{\odot}\text{pc}^{-2}$. Our virial equilibrium analysis suggests that these CO-bright H I clouds are gravitationally bound or marginally bound.

We also found an anti-correlation between molecular mass fractions and Galactocentric distances, as well as a

correlation between molecular mass fractions and total gas surface densities. Among the CO-bright H I superclouds, nine are associated with H II regions, indicating ongoing star formation. The star-forming H I superclouds have molecular mass fractions larger than 0.1, although some H I superclouds that meet this criterion do not match with H II regions.

Consistent with previous studies, we showed that H I superclouds are regularly spaced along the spiral arm, with a typical spacing of $0.084 R_0$ (~ 700 pc); this could be partly a selection effect from blending at short spacings. The presence of a peak in the ratio of separation to the minor axis, which closely aligns with the theoretical expectation of 3.9, suggests that the observed regular spacing is not a result of chance but rather an outcome of an underlying physical process. We observed a strong spatial correlation between H II regions and molecular clouds, with some offsets between molecular clouds and local H I column density peaks.

Lastly, we examined the relationship between the SFR surface density and surface densities of H I, H₂, and to-

tal gas. In agreement with extragalactic studies of the resolved K-S relation and local GMCs study by Lada et al. (2013), our results indicate that Σ_{SFR} is independent of Σ_{HI} and $\Sigma_{\text{HI+H}_2}$, but show a positive correlation with Σ_{H_2} with a power-law index of ~ 1.3 . This consistency with the well-established value of ~ 1.4 for the global K-S relation highlights the significant role molecular gas plays in controlling star formation and lends further credence to the K-S relation as a key scaling law that governs the transformation of gas into stars.

- 1 G.P. was supported by the National Research
- 2 Foundation of Korea through grants NRF-
- 3 2020R1A6A3A01100208 and RS-2023-00242652. This
- 4 work was partly supported by the Korea Astronomy
- 5 and Space Science Institute grant funded by the Korea
- 6 government(MSIT) (Project No. 2022-1-840-05).

Software: ASTROML (VanderPlas et al. 2012; Ivezić et al. 2014), The IDL Astronomy User’s Library (Landsman 1993)

REFERENCES

- Abdo, A. A., Ackermann, M., Ajello, M., et al. 2010, ApJ, 710, 133, doi: [10.1088/0004-637X/710/1/133](https://doi.org/10.1088/0004-637X/710/1/133)
- Allen, C. W. 1973, Astrophysical quantities
- Anderson, L. D., Bania, T. M., Balsler, D. S., et al. 2014, ApJS, 212, 1, doi: [10.1088/0067-0049/212/1/1](https://doi.org/10.1088/0067-0049/212/1/1)
- Ballesteros-Paredes, J., Hartmann, L., & Vázquez-Semadeni, E. 1999, ApJ, 527, 285, doi: [10.1086/308076](https://doi.org/10.1086/308076)
- Barriault, L., Joncas, G., Lockman, F. J., & Martin, P. G. 2010, MNRAS, 407, 2645, doi: [10.1111/j.1365-2966.2010.17105.x](https://doi.org/10.1111/j.1365-2966.2010.17105.x)
- Bigiel, F., Leroy, A., Walter, F., et al. 2008, AJ, 136, 2846, doi: [10.1088/0004-6256/136/6/2846](https://doi.org/10.1088/0004-6256/136/6/2846)
- Blitz, L. 1993, in Protostars and Planets III, ed. E. H. Levy & J. I. Lunine, 125
- Bolatto, A. D., Wolfire, M., & Leroy, A. K. 2013, ARA&A, 51, 207, doi: [10.1146/annurev-astro-082812-140944](https://doi.org/10.1146/annurev-astro-082812-140944)
- Boulanger, F., & Viallefond, F. 1992, A&A, 266, 37
- Burton, W. B. 1988, in Galactic and Extragalactic Radio Astronomy, ed. K. I. Kellermann & G. L. Verschuur, 295–358
- Chandrasekhar, S., & Fermi, E. 1953, ApJ, 118, 116, doi: [10.1086/145732](https://doi.org/10.1086/145732)
- Cowie, L. 1981, ApJ, 245, 66, doi: [10.1086/158786](https://doi.org/10.1086/158786)
- Dame, T. M., Hartmann, D., & Thaddeus, P. 2001, ApJ, 547, 792, doi: [10.1086/318388](https://doi.org/10.1086/318388)
- Dobbs, C. 2008, MNRAS, 391, 844–858, doi: [10.1111/j.1365-2966.2008.13939.x](https://doi.org/10.1111/j.1365-2966.2008.13939.x)
- Dobbs, C., Glover, S., Clark, P., & Klessen, R. S. 2008, MNRAS, 389, 1097, doi: [10.1111/j.1365-2966.2008.13646.x](https://doi.org/10.1111/j.1365-2966.2008.13646.x)
- Dobbs, C. L., Krumholz, M. R., Ballesteros-Paredes, J., et al. 2014, in Protostars and Planets VI, ed. H. Beuther, R. S. Klessen, C. P. Dullemond, & T. Henning, 3–26, doi: [10.2458/azu_uapress.9780816531240-ch001](https://doi.org/10.2458/azu_uapress.9780816531240-ch001)
- Efremov, Y. N. 1998, Astronomical and Astrophysical Transactions, 15, 3, doi: [10.1080/10556799808201745](https://doi.org/10.1080/10556799808201745)
- . 2009, Astronomy Letters, 35, 507, doi: [10.1134/S1063773709080015](https://doi.org/10.1134/S1063773709080015)
- . 2010, MNRAS, 405, 1531, doi: [10.1111/j.1365-2966.2010.16578.x](https://doi.org/10.1111/j.1365-2966.2010.16578.x)
- Elmegreen, B. G. 1979, ApJ, 231, 372
- . 1982, ApJ, 253, 655, doi: [10.1086/159666](https://doi.org/10.1086/159666)
- Elmegreen, B. G. 1996, in Unsolved Problems of the Milky Way, ed. L. Blitz & P. J. Teuben, Vol. 169, 551
- . 2004, arXiv e-prints, astro, doi: [10.48550/arXiv.astro-ph/0411282](https://doi.org/10.48550/arXiv.astro-ph/0411282)
- Elmegreen, B. G., & Clemens, C. 1985, ApJ, 294, 523, doi: [10.1086/163320](https://doi.org/10.1086/163320)
- Elmegreen, B. G., & Elmegreen, D. M. 1983, MNRAS, 203, 31, doi: [10.1093/mnras/203.1.31](https://doi.org/10.1093/mnras/203.1.31)
- . 1987, ApJ, 320, 182, doi: [10.1086/165534](https://doi.org/10.1086/165534)

- . 2019, *ApJS*, 245, 14, doi: [10.3847/1538-4365/ab4903](https://doi.org/10.3847/1538-4365/ab4903)
- Elmegreen, B. G., Elmegreen, D. M., & Efremov, Y. N. 2018, *ApJ*, 863, 59, doi: [10.3847/1538-4357/aacf9a](https://doi.org/10.3847/1538-4357/aacf9a)
- Engargiola, G., Plambeck, R. L., Rosolowsky, E., & Blitz, L. 2003, *ApJS*, 149, 343, doi: [10.1086/379165](https://doi.org/10.1086/379165)
- Fiege, J. D., & Pudritz, R. E. 2000, *MNRAS*, 311, 105, doi: [10.1046/j.1365-8711.2000.03067.x](https://doi.org/10.1046/j.1365-8711.2000.03067.x)
- Fukui, Y., & Kawamura, A. 2010, *ARA&A*, 48, 547, doi: [10.1146/annurev-astro-081309-130854](https://doi.org/10.1146/annurev-astro-081309-130854)
- Grabelsky, D. A., Cohen, R. S., Bronfman, L., Thaddeus, P., & May, J. 1987, *ApJ*, 315, 122, doi: [10.1086/165118](https://doi.org/10.1086/165118)
- Grenier, I. A., Casandjian, J.-M., & Terrier, R. 2005, *Science*, 307, 1292, doi: [10.1126/science.1106924](https://doi.org/10.1126/science.1106924)
- Gusev, A., Shimanovskaya, E., & Zaitseva, N. 2022, *MNRAS*, 514, 3953–3964, doi: doi.org/10.1093/mnras/stac1592
- Hartmann, L., Ballesteros-Paredes, J., & Bergin, E. A. 2001, *ApJ*, 562, 852, doi: [10.1086/323863](https://doi.org/10.1086/323863)
- Hennebelle, P., & Pérault, M. 2000, *A&A*, 359, 1124
- Heyer, M., Krawczyk, C., Duval, J., & Jackson, J. M. 2009, *ApJ*, 699, 1092, doi: [10.1088/0004-637X/699/2/1092](https://doi.org/10.1088/0004-637X/699/2/1092)
- HI4PI Collaboration, Ben Bekhti, N., Flöer, L., et al. 2016, *A&A*, 594, A116, doi: [10.1051/0004-6361/201629178](https://doi.org/10.1051/0004-6361/201629178)
- Ianjamasimanana, R., de Blok, W., Walter, F., & Heald, G. 2012, *ApJ*, 144, 96 (25pp), doi: [10.1088/0004-6256/144/4/96](https://doi.org/10.1088/0004-6256/144/4/96)
- Inoue, S., & Yoshida, N. 2019, *MNRAS*, 485, 3024, doi: [10.1093/mnras/stz584](https://doi.org/10.1093/mnras/stz584)
- Inoue, T., & Inutsuka, S.-i. 2009, *ApJ*, 704, 161, doi: [10.1088/0004-637X/704/1/161](https://doi.org/10.1088/0004-637X/704/1/161)
- Inutsuka, S.-i., Inoue, T., Iwasaki, K., & Hosokawa, T. 2015, *A&A*, 580, A49, doi: [10.1051/0004-6361/201425584](https://doi.org/10.1051/0004-6361/201425584)
- Inutsuka, S.-I., & Miyama, S. M. 1992, *ApJ*, 388, 392, doi: [10.1086/171162](https://doi.org/10.1086/171162)
- Ivezić, Ž., Connolly, A. J., VanderPlas, J. T., & Gray, A. 2014, *Statistics, Data Mining, and Machine Learning in Astronomy: A Practical Python Guide for the Analysis of Survey Data*, doi: [10.1515/9781400848911](https://doi.org/10.1515/9781400848911)
- Kalberla, P. M. W., Burton, W. B., Hartmann, D., et al. 2005, *A&A*, 440, 775, doi: [10.1051/0004-6361:20041864](https://doi.org/10.1051/0004-6361:20041864)
- Kalberla, P. M. W., & Haud, U. 2015, *A&A*, 578, A78, doi: [10.1051/0004-6361/201525859](https://doi.org/10.1051/0004-6361/201525859)
- Kalberla, P. M. W., McClure-Griffiths, N. M., Pisano, D. J., et al. 2010, *A&A*, 521, A17, doi: [10.1051/0004-6361/200913979](https://doi.org/10.1051/0004-6361/200913979)
- Kennicutt, Robert C., J. 1989, *ApJ*, 344, 685, doi: [10.1086/167834](https://doi.org/10.1086/167834)
- . 1998, *ApJ*, 498, 541, doi: [10.1086/305588](https://doi.org/10.1086/305588)
- Kennicutt, R. C., & Evans, N. J. 2012, *ARA&A*, 50, 531, doi: [10.1146/annurev-astro-081811-125610](https://doi.org/10.1146/annurev-astro-081811-125610)
- Kerp, J., Winkel, B., Ben Bekhti, N., Flöer, L., & Kalberla, P. M. W. 2011, *Astronomische Nachrichten*, 332, 637, doi: [10.1002/asna.201011548](https://doi.org/10.1002/asna.201011548)
- Kim, W.-T., Ostriker, E. C., & Stone, J. M. 2002, *ApJ*, 581, 1080
- Koda, J., Scoville, N., & Heyer, M. 2016, *ApJ*, 823, 76, doi: [10.3847/0004-637X/823/2/76](https://doi.org/10.3847/0004-637X/823/2/76)
- Koo, B.-C., Park, G., Kim, W.-T., et al. 2017, *PASP*, 129, 094102 (Paper I), doi: [10.1088/1538-3873/aa7c08](https://doi.org/10.1088/1538-3873/aa7c08)
- Krumholz, M. R., McKee, C. F., & Tumlinson, J. 2009, *ApJ*, 693, 216, doi: [10.1088/0004-637X/693/1/216](https://doi.org/10.1088/0004-637X/693/1/216)
- Kwan, J., & Valdes, F. 1987, *ApJ*, 315, 92, doi: [10.1086/165116](https://doi.org/10.1086/165116)
- Lada, C. J., Lombardi, M., Roman-Zuniga, C., Forbrich, J., & Alves, J. F. 2013, *ApJ*, 778, 133, doi: [10.1088/0004-637X/778/2/133](https://doi.org/10.1088/0004-637X/778/2/133)
- Lada, C. J., Margulis, M., Sofue, Y., Nakai, N., & Handa, T. 1988, *ApJ*, 328, 143, doi: [10.1086/166275](https://doi.org/10.1086/166275)
- Landsman, W. B. 1993, in *Astronomical Society of the Pacific Conference Series*, Vol. 52, *Astronomical Data Analysis Software and Systems II*, ed. R. J. Hanisch, R. J. V. Brissenden, & J. Barnes, 246
- Lee, E. J., Murray, N., & Rahman, M. 2012a, *ApJ*, 752, 146, doi: [10.1088/0004-637X/752/2/146](https://doi.org/10.1088/0004-637X/752/2/146)
- Lee, M.-Y., Stanimirović, S., Murray, C. E., Heiles, C., & Miller, J. 2015, *ApJ*, 809, 56, doi: [10.1088/0004-637X/809/1/56](https://doi.org/10.1088/0004-637X/809/1/56)
- Lee, M.-Y., Stanimirović, S., Douglas, K. A., et al. 2012b, *ApJ*, 748, 75, doi: [10.1088/0004-637X/748/2/75](https://doi.org/10.1088/0004-637X/748/2/75)
- Lee, S. M., & Hong, S. S. 2011, *ApJ*, 734, 101, doi: [10.1088/0004-637X/734/2/101](https://doi.org/10.1088/0004-637X/734/2/101)
- Leroy, A. K., Walter, F., Brinks, E., et al. 2008, *AJ*, 136, 2782, doi: [10.1088/0004-6256/136/6/2782](https://doi.org/10.1088/0004-6256/136/6/2782)
- Leroy, A. K., Walter, F., Sandstrom, K., et al. 2013, *AJ*, 146, 19, doi: [10.1088/0004-6256/146/2/19](https://doi.org/10.1088/0004-6256/146/2/19)
- Levine, E. S., Blitz, L., & Heiles, C. 2006, *ApJ*, 643, 881, doi: [10.1086/503091](https://doi.org/10.1086/503091)
- Liszt, H. 2014, *ApJ*, 783, 17, doi: [10.1088/0004-637X/783/1/17](https://doi.org/10.1088/0004-637X/783/1/17)
- Liszt, H., & Lucas, R. 1996, *A&A*, 314, 917
- Lombardi, M., Alves, J., & Lada, C. J. 2010, *A&A*, 519, L7, doi: [10.1051/0004-6361/201015282](https://doi.org/10.1051/0004-6361/201015282)
- Lucas, R., & Liszt, H. 1996, *A&A*, 307, 237
- Mandowara, Y., Sormani, M. C., Sobacchi, E., & Klessen, R. 2022, *MNRAS*, 513, 5052, doi: [10.1093/mnras/stac1214](https://doi.org/10.1093/mnras/stac1214)

- Markwardt, C. B. 2009, in *Astronomical Society of the Pacific Conference Series*, Vol. 411, *Astronomical Data Analysis Software and Systems XVIII*, ed. D. A. Bohlender, D. Durand, & P. Dowler, 251, doi: [10.48550/arXiv.0902.2850](https://doi.org/10.48550/arXiv.0902.2850)
- McClure-Griffiths, N. M., Dickey, J. M., Gaensler, B. M., & Green, A. J. 2002, *ApJ*, 578, 176, doi: [10.1086/342470](https://doi.org/10.1086/342470)
- McClure-Griffiths, N. M., Dickey, J. M., Gaensler, B. M., et al. 2005, *ApJS*, 158, 178, doi: [10.1086/430114](https://doi.org/10.1086/430114)
- McClure-Griffiths, N. M., Pisano, D. J., Calabretta, M. R., et al. 2009, *ApJS*, 181, 398, doi: [10.1088/0067-0049/181/2/398](https://doi.org/10.1088/0067-0049/181/2/398)
- McGee, R. X., & Milton, J. A. 1964, *Australian Journal of Physics*, 17, 128, doi: [10.1071/PH640128](https://doi.org/10.1071/PH640128)
- Meyerdierks, H., & Heithausen, A. 1996, *A&A*, 313, 929
- Mezger, P. O. 1978, *A&A*, 70, 565
- Murray, N., & Rahman, M. 2010, *ApJ*, 709, 424, doi: [10.1088/0004-637X/709/1/424](https://doi.org/10.1088/0004-637X/709/1/424)
- Nagasawa, M. 1987, *Progress of Theoretical Physics*, 77, 635, doi: [10.1143/PTP.77.635](https://doi.org/10.1143/PTP.77.635)
- Ostriker, E. C., & Kim, W. T. 2004, in *Astronomical Society of the Pacific Conference Series*, Vol. 317, *Milky Way Surveys: The Structure and Evolution of our Galaxy*, ed. D. Clemens, R. Shah, & T. Brainerd, 248
- Ostriker, J. 1964, *ApJ*, 140, 1056, doi: [10.1086/148005](https://doi.org/10.1086/148005)
- Park, G., Koo, B.-C., Kim, K.-T., Byun, D.-Y., & Heiles, C. E. 2018, *Ap&SS*, 363, 150, doi: [10.1007/s10509-018-3372-4](https://doi.org/10.1007/s10509-018-3372-4)
- Pedicelli, S., Bono, G., Lemasle, B., et al. 2009, *A&A*, 504, 81, doi: [10.1051/0004-6361/200912504](https://doi.org/10.1051/0004-6361/200912504)
- Pineda, J. L., Langer, W. D., Velusamy, T., & Goldsmith, P. F. 2013, *A&A*, 554, A103, doi: [10.1051/0004-6361/201321188](https://doi.org/10.1051/0004-6361/201321188)
- Planck Collaboration, Abergel, A., Ade, P. A. R., et al. 2011a, *A&A*, 536, A24, doi: [10.1051/0004-6361/201116485](https://doi.org/10.1051/0004-6361/201116485)
- Planck Collaboration, Ade, P. A. R., Aghanim, N., et al. 2011b, *A&A*, 536, A19, doi: [10.1051/0004-6361/201116479](https://doi.org/10.1051/0004-6361/201116479)
- Reach, W. T., Koo, B.-C., & Heiles, C. 1994, *ApJ*, 429, 672, doi: [10.1086/174353](https://doi.org/10.1086/174353)
- Reid, M. J., & Dame, T. M. 2016, *ApJ*, 832, 159, doi: [10.3847/0004-637X/832/2/159](https://doi.org/10.3847/0004-637X/832/2/159)
- Reid, M. J., Menten, K. M., Brunthaler, A., et al. 2014, *ApJ*, 783, 130, doi: [10.1088/0004-637X/783/2/130](https://doi.org/10.1088/0004-637X/783/2/130)
- Renaud, F., Bournaud, F., Emsellem, E., et al. 2013, *MNRAS*, 436, 1836, doi: [10.1093/mnras/stt1698](https://doi.org/10.1093/mnras/stt1698)
- Schmidt, M. 1959, *ApJ*, 129, 243, doi: [10.1086/146614](https://doi.org/10.1086/146614)
- Schruba, A., Leroy, A. K., Walter, F., et al. 2011, *AJ*, 142, 37, doi: [10.1088/0004-6256/142/2/37](https://doi.org/10.1088/0004-6256/142/2/37)
- Stodólkiewicz, J. S. 1963, *AcA*, 13, 30
- Tang, N., Li, D., Heiles, C., et al. 2017, *ApJ*, 839, 8, doi: [10.3847/1538-4357/aa67e9](https://doi.org/10.3847/1538-4357/aa67e9)
- Tosaki, T., Kuno, N., Onodera, Sachiko Miura, R., et al. 2011, *PASJ*, 63, 1171, doi: [10.1093/pasj/63.6.1171](https://doi.org/10.1093/pasj/63.6.1171)
- van Dishoeck, E. F., & Black, J. H. 1988, *ApJ*, 334, 771, doi: [10.1086/166877](https://doi.org/10.1086/166877)
- VanderPlas, J., Connolly, A. J., Ivezić, Z., & Gray, A. 2012, in *Proceedings of Conference on Intelligent Data Understanding (CIDU)*, 47–54, doi: [10.1109/CIDU.2012.6382200](https://doi.org/10.1109/CIDU.2012.6382200)
- Wada, K., & Koda, J. 2004, *MNRAS*, 349, 270–280, doi: [110.1111/j.1365-2966.2004.07484.x](https://doi.org/10.1111/j.1365-2966.2004.07484.x)
- Wegg, C., Gerhard, O., & Portail, M. 2015, *MNRAS*, 450, 4050, doi: [10.1093/mnras/stv745](https://doi.org/10.1093/mnras/stv745)
- Williams, J. P., de Geus, E. J., & Blitz, L. 1994, *ApJ*, 428, 693, doi: [10.1086/174279](https://doi.org/10.1086/174279)
- Williams, T. G., Gear, W. K., & Smith, M. W. L. 2018, *MNRAS*, 479, 297, doi: [10.1093/mnras/sty1476](https://doi.org/10.1093/mnras/sty1476)
- Winkel, B., Kerp, J., Flöer, L., et al. 2016, *A&A*, 585, A41, doi: [10.1051/0004-6361/201527007](https://doi.org/10.1051/0004-6361/201527007)
- Wolfire, M. G., Hollenbach, D., & McKee, C. F. 2010, *ApJ*, 716, 1191, doi: [10.1088/0004-637X/716/2/1191](https://doi.org/10.1088/0004-637X/716/2/1191)
- Wong, T., & Blitz, L. 2002, *ApJ*, 569, 157, doi: [10.1086/339287](https://doi.org/10.1086/339287)
- Wong, T., Hughes, A., Fukui, Y., et al. 2009, *ApJ*, 696, 370, doi: [10.1088/0004-637X/696/1/370](https://doi.org/10.1088/0004-637X/696/1/370)